Electrohydrodynamic interaction, deformation, and coalescence of suspended drop pairs at varied angle of incidence

Qingming Dong and Amalendu Sau*
Department of Aerospace and Software Engineering, Gyeongsang National University, Jinju 660701, Republic of Korea

(Received 2 January 2018; published 9 July 2018)

The electrohydrodynamic interaction of liquid drop pairs suspended in another immiscible liquid and subjected to uniform electric field is examined using the leaky dielectric model and the explicit forcing lattice Boltzmann method, by taking into account the nonlinear inertia effects. This facilitates explorations of wider parametric contrast, precise electrohydrodynamic interaction, and postcoalescence breakup phenomena that remained unknown. The influence of dielectrophoretic and electrohydrodynamic forces in *prolate*- and *oblate*-shaped deformations, coalescences, and repulsive motion of leaky drop pairs appearing at widely varied incidence angle ($\alpha \geqslant 0^\circ$) to the applied electric field is studied. The electrically driven flow at $\alpha = 0^\circ$ evolves in the form of decisively important *outflow*- and *inflow*-natured counterrotating vortex pairs in and around the drops. With suitably tuned conductivity (σ_{in}/σ_{out}) and permittivity ($\varepsilon_{in}/\varepsilon_{out}$) ratios of drop fluid to surrounding outer medium, the relative impacts of attractive electric force versus *outflow*- or *inflow*-natured vortex pair-induced hydrodynamic force was optimized to distinctly facilitate the *prolate*- and the *oblate*-type deformations of a drop pair, their coalescence, departure, and the postcoalescence breakup. For varied $\varepsilon_{in}/\varepsilon_{out}$ over a range $0.25 \leqslant \varepsilon_{in}/\varepsilon_{out} \leqslant 20.0$, and using fixed conductivity ratio $\sigma_{in}/\sigma_{out} = 5.0$ and electric capillary number $\mathrm{Ca}_E = 0.46$ (the ratio of electric force and surface tension), the dipolar electric force is appropriately set with respect to the surrounding four *outflow*-type outer vortex pair-induced hydrodynamic force to enforce two *prolately* deformed drops move apart for $\varepsilon_{in}/\varepsilon_{out} < (\varepsilon_{in}/\varepsilon_{out})_{crit1} \approx 2.4$ and coalesce for $2.4 < \varepsilon_{in}/\varepsilon_{out} < 9.57$. The low pressure that grew at the neck of near-contact or coalescing drops facilitated the transport of inner fluid into neck region and helped the drop pair's coalescence. For $\varepsilon_{in}/\varepsilon_{out} > (\varepsilon_{in}/\varepsilon_{out})_{crit3} \approx 9.57$, exceeding a critical value, the deformed *oblate* drop pair moved closer and coalesced; and depending on $\varepsilon_{in}/\varepsilon_{out}$ the coalesced drop subsequently broke into a number of satellite or daughter drops spread in a direction perpendicular to the electric field; and such a phenomenon is newly identified. For the nonaligned drop pairs with $\alpha < 54.7^\circ$ or $\alpha > 125.3^\circ$, the attractive radial ($\boldsymbol{F_r}$) component of dielectrophoretic force drove two drops closer, while the torque produced by tangential ($\boldsymbol{F_t}$) components of the electric force made them rotate and align to the electric field upon coalescence. For $54.7^\circ < \alpha < 125.3^\circ$ the dipolar radial force ($\boldsymbol{F_r}$) appeared repulsive and drop pair moved apart. Importantly for nonaligned drop pairs both *oblate* and *prolate* deformations are noticed, for suitably selected dielectric properties.

DOI: 10.1103/PhysRevFluids.3.073701

I. INTRODUCTION

The response of immiscible conducting liquid drops under applied electric field brings in promising means of phase separation or transporting liquids in the form of droplets, which include

*amalendu.sau@gmail.com

dewatering of crude oil via electrocoalescence [1,2], augmentation of electroconvection [3,4], fuel atomization [5], electrospray mass spectrometry [6], and important biotechnological applications [7]. In addition, in many microfluidic devices the electric field is utilized to control migration, targeted coalescence, and fission of surfactant stabilized drops, as microreactors, for facilitating mixing of reagents in biological or chemical assays [8]. The fundamental need of investigating drop's responses to an electric field is to extract decisive information on how to efficiently manipulate the behavior of drops for practical purposes. Moreover, depending on the angle of incidence α of two polarized drops in an electric field, the attractive- or repulsive-natured force develops via dipole-dipole interaction. The phenomenon is known as dielectrophoretic effect; and it leads to *coalescence or divergence* of emulsion drops. For a pair of leaky dielectric drops suspended in a leaky dielectric emulsion, using full nonlinear governing equations the present study shows that the electrohydrodynamic (EHD) flow developed due to interactive tangential electric stress at drop interface facilitates the systematic *outflow* and *inflow* paired vortex dynamics-induced forcing, structural distortion, and breakup of a coalesced drop in a direction orthogonal to applied electric field. Accordingly, drops deform *prolately* or *oblately* and move *closer* or *apart* depending upon chosen conductivity and permittivity ratios of drop fluid and surrounding fluid.

Considering relatively poor conductive behavior of fluids, the leaky dielectric model of Taylor [9] predicts the deformation and internal kinetics of a *single drop* suspended in another immiscible fluid, when subjected to an external electric field. Due to low conductivity, a small amount of electric current develops on the drop under the influence of the applied electric field and facilitates the surface charge built up along the periphery. The accumulated charges effectively modify the local field strength and help growth of the tangential component of electrical shear force along a charged drop interface, in addition to electric pressure. The tangential electric shear force in turn drags neighboring bulk fluid into motion that helps creating the dynamically important near-surface vortex pairs. The resulting physical interaction accordingly affects the interfacial stability and spreading of the leaky dielectric drops *via* the symmetrically paired vortex motion-induced thrust. While the accompanying interface distortion coupled with surface tension balance the normal component of the electric stress, the tangential electric shear stress contributes to *oblate*- or *prolate*-type drop deformations. Based on Taylor's leaky dielectric model [9], efforts have been made over the past years to examine EHD problems both experimentally [10] and theoretically [11–16] to understand response of various emulsion drops in externally applied electric field. Notably, the experimental study of Torza *et al.* [10] exhibits the growth of the *oblate- and prolate*-shaped drops depending on varied fluid properties (permittivity and conductivity) that facilitated small deformation. Moreover, for large nonlinear deformations the reported deviation from the linear theory is effectively resolved with the inclusion of the higher order terms [11] in the original asymptotic model [9]. The recent finding of Lac and Homsy [12] supports such a conjecture, and the authors extend their investigation to explore the drop's approach to different breaking modes in the Stokes regime. The influence of the viscosity contrast on the instability or breakup of a drop is theoretically addressed by Lac and Homsy [12]. In addition, the past researchers [17,18] elaborate important influences of the EHD vortices around a leaky dielectric drop, when exposed to an external electric field.

However, multiple drop dispersion is encountered [19–25] in many practical applications. For aligned *two-drop system*, the *asymmetric* electric field, compared to a *symmetric* state that persists with an isolated drop, is produced due to presence of the neighboring drop. The phenomenon that the intensity of the electric field at one side of a drop is stronger than that at another side is the well-known *dielectrophoresis* effect [20]. Based on the dipole argument, Atten [21] examined electric interaction between two close emulsion drops in the form of electrostatic forces located at drop centers. For small separation distance, Atten *et al.* [22] show that the nondimensional critical distance for two drops that can facilitate coalescence is $s_{\text{crit}}/R_0 \approx 0.63 s_0/R_0$ and the critical magnitude of applied electric field $E_{\text{crit}} \sim s_0^{1.30}$, where s_0 is the distance and R_0 is radius of the undistorted drops aligned along the direction of the electric field. Moreover, Bird *et al.* [23] show that, above a critical electric capillary number (Ca_E) a drop pair aligned to an electric field does not always coalesce even after contact, and they attribute the process to the *cone angle and pressure gradient* that form at the neck

region. On the other hand, recently Eow and Ghadiri [24] experimentally examined response of a pair of suspended drops at varied inclination α with the applied electric field and observed *mutual attraction and repulsion* behaviors, depending on the angle α between the electric field and the line joining mass centers of two drops. Later, Mhatre *et al.* [25] examined the electrocoalescence of two drops. However, the precise electrohydrodynamic interaction, possible *prolate*- or *oblate*-shaped deformation of nonaligned drops ($\alpha > 0^\circ$), and decisive governing physics that impacts coalescence or repulsion remained practically unknown. The present study aims to add significantly to the existing knowledge of electrocoalescence plus postcoalescence breakup of a leaky dielectric drop pair by appropriately analyzing the competitive roles of electric force and electrically induced hydrodynamic influence *via* the created *inflow and outflow* paired *vortex dynamics*, by using widely varied electric field strength, fluid properties, and incidence angle α.

Notably, using the Navier-Stokes equation, Hua *et al.* [15] shows that for an *isolated* leaky dielectric drop the *symmetrically paired* vortical flow that develops in the near-field practically balances the tangential component of interfacial electric stress. However, for *two adjacent drops* in proximity the imbalance created by electrically induced a*symmetrical* vortical flow plus developed pressure gradient (e.g., Bird *et al.* [23]) around one drop can have significant impact on the other drop. Based on creeping flow conditions and far-field argument Baygents *et al.* [26] postulate a kind of hydrodynamic interaction for two leaky dielectric drops aligned to ($\alpha = 0^\circ$) an external electric field, where bulk fluid motion produced by the tangential electric stress is thought to influence a drop pair move *closer or apart* depending on the *sense of near-surface circulation*. However, the role of important *outflow*-natured near-interface vortex pairs remained practically unknown. Moreover, Zhang *et al.* [27] investigated the collision or coalescence of two *conducting* drops using a trajectory analysis. Although, unlike with leaky drops suspended in leaky dielectric fluid, the electrically driven near-interface vortices were absent for the conducting drops [27] placed in a perfect dielectric fluid. Accordingly, the electrically driven hydrodynamic interaction was not explored in previous studies [28–30], as authors addressed issues related to perfect conductors or perfect dielectrics. Hereby unambiguous and clear evidences are provided to reveal how exactly the EHD interaction generated *inflow and outflow* paired near-field vortical motion in leaky dielectrics plays a competitive or supporting role together with the electric interaction to control the drop pair's *dynamics*, *prolate*- or *oblate-type deformations*, and *coalescences*, over a wide range of incidence angle α. Moreover, the present nonlinear model captures the new modes of postcoalescing breakup of a pair of leaky drops at $\alpha = 0^\circ$, for sufficiently high electric capillary number (Ca_E).

To reveal the governing flow interaction, an improved explicit forcing lattice Boltzmann method (LBM) is employed hereby. The mesoscopic approach [31,32] has benefit that the evolving interfaces do not require special tracking or reconstruction at each time step and arise naturally as the part of adopted liquid-liquid phase separation model. Instead of Shan and Chen [33] model, in this study we have employed the improved explicit forcing model of Porter *et al.* [34]. The LB model of Porter *et al.* [34] uses higher-order isotropy in the evaluation of fluid-fluid forces and reduces the magnitude of spurious currents in vicinity of the interface. The relative performances of the above said two models are also extensively demonstrated, as appeared appropriate. The detailed theoretical background for the EHD interaction and the implementation of the LBM are presented in Sec. II. Subsequently, in Sec. III, the computation of the droplet's surface tension is elaborated. This is followed by extensive validation of the adopted solution algorithm, showing comparison our simulated results with the available recent theoretical or numerical results for an isolated drop [12,14,50], and with results reported for a coalescing drop pair [25] using boundary element method (BEM). Thereafter, the motion or deformation of leaky dielectric drop pairs are systematically investigated first, as they remained aligned ($\alpha = 0^\circ$) with the applied electric field. Using varied field properties, the important driving factors are ascertained in order to demonstrate relative roles of electric interaction and paired vortex dynamics-induced hydrodynamic interaction. Finally, the effect of varied inclination α of two suspended nonaligned drops on their rotating motion, *prolate- or oblate*-type *coalescences*, *and drifting* are systematically explored to present a comprehensive understanding of the physical scenarios.

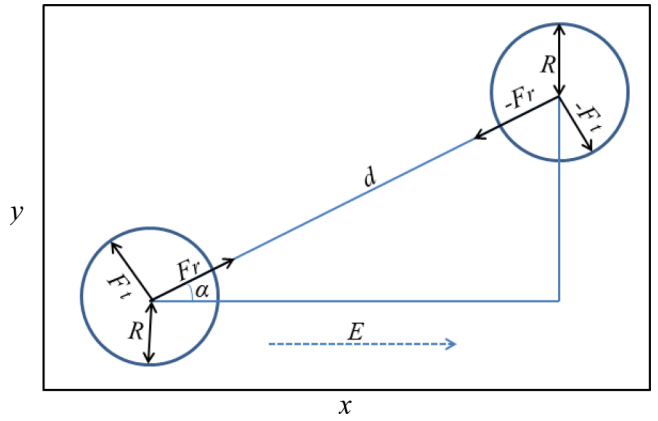

FIG. 1. Sketch of two identical drops appearing at an angle α to the electric field E and placed at a distance d apart. The radial (F_r) and tangential (F_t) components of the induced electric force are shown to act at respective drop centers.

II. THE GOVERNING EQUATION AND THE NUMERICAL METHOD

The important work of Baygents *et al.* [26] is followed to formulate the model problem. However, instead of solving Stokes equation, hereby full nonlinear effects are taken into account to explore precise flow interactions and governing physics. We consider two uncharged liquid drops of identical property and radius R (Fig. 1), placed in an immiscible liquid subjected to uniform electric field E. The liquids inside and outside the drops are assumed incompressible (of equal density ρ), Newtonian, and leaky dielectrics [35], and have viscosities μ_{in}, μ_{out}, permittivities ε_{in}, ε_{out}, and conductivities σ_{in}, σ_{out}, respectively. The initial center-to-center separation distance of two drops is d, and the interfaces separating two immiscible fluids have constant surface tension γ. Here we ignore the impacts of gravitational force and buoyancy effect.

A. The leaky dielectric model

The leaky dielectric theory of Taylor [9] and Melcher and Taylor [35] is used here to model the electrical response of the suspended drops in a surrounding fluid medium. For the investigated dielectric-dielectric system the magnetic induction effect is ignored, and electrostatic equations become an accurate approximation. Since the propagation time for electromagnetic waves is much faster compared to characteristic timescale of the induced hydrodynamic motion, the small ionic charges are assumed to be present only at interface, and the concept of diffuse (Debye) layers (volumetric charges) becomes irrelevant. Accordingly, the electrical phenomena are governed by

$$\nabla \times \vec{E} = 0. \tag{1}$$

Moreover, Gauss's law in a dielectric fluid medium of permittivity ε, when written in terms of electric displacement $\vec{D}(=\varepsilon\vec{E})$, becomes the following [Eq. (2)], where q_v denotes the volume density of free charge:

$$\nabla \cdot \vec{D} = \nabla \cdot (\varepsilon \vec{E}) = q_v. \tag{2}$$

Additionally, the charge conservation equation is expressed as

$$\nabla \cdot \vec{J} + \frac{Dq_v}{Dt} = \nabla \cdot (\sigma \vec{E}) + \frac{\partial q_v}{\partial t} + \vec{u} \cdot \nabla q_v = 0, \tag{3}$$

where $\vec{J} = \sigma\vec{E}$ is the current density due to conduction, σ is the electrical conductivity, D/Dt denotes the material derivative, and $\vec{u}$ is the local fluid velocity. Inserting Eq. (2) into Eq. (3), one

obtains

$$q_v = q_{v,0} e^{-\frac{\sigma}{\varepsilon} t}, \tag{4}$$

where subscript 0 represents the initial time, and a field variable χ above corresponds to both χ_{in} and χ_{out}.

Equation (4) shows the charge density in the neighborhood of a fluid particle decays with relaxation time $t_e = \varepsilon/\sigma$. The hydrodynamic timescale for the motion is given by $t_v = \rho R^2/\mu$. Based on Melcher and Taylor's theory [35], for a conductive fluid with $t_e \ll t_v$, any existing free charge instantly accumulates at interface and charge conservation occurs faster than fluid response. Consequently, for a leaky dielectric model, the free charge in bulk fluid is zero and the charge is constrained on the surface, that is $Dq_v/Dt = 0$, and Eq. (3) becomes

$$\nabla \cdot (\sigma \vec{E}) = 0. \tag{5}$$

Moreover, in terms of the electric potential (V), the electric field strength can be written as

$$\vec{E} = -\nabla V. \tag{6}$$

Combining Eqs. (5) and (6), the governing equation for the electric field (potential) can be obtained as

$$\nabla \cdot (\sigma \nabla V) = 0. \tag{7}$$

On a fluid-fluid interface the electric potential (V) and the tangential component of the local electric filed ($\boldsymbol{E}$) are assumed continuous,

$$\vec{t} \cdot \vec{E}_{\text{in}} = \vec{t} \cdot \vec{E}_{\text{out}}, \quad V_{\text{in}} = V_{\text{out}}, \tag{7a}$$

where $\vec{t}$ is the unit tangent vector at the interface.

However, owing to mismatching electrical property of inner and outer fluids, the jump of normal component of local electric field generates surface charge $q(\vec{x})$, that is calculated through Gauss's law,

$$q(\vec{x}) = [\![\varepsilon \vec{E}_x]\!] \quad \text{for } x \in S, \tag{7b}$$

where, $[\![\cdot]\!]$ denotes jump across the interface, and S denotes droplet surface. Over the years two methods are employed [12,14,15,27,36,37] to describe the surface charge. One method takes into account the Ohmic current from the bulk and advection by fluid flow on the drop surface. Therefore, it is governed by the following charge conservation equation [36,37]:

$$\frac{\partial q}{\partial t} + [\![\sigma \vec{E}_n]\!] + \nabla_S \cdot (q\vec{v}) = 0 \quad \text{for } x \in S, \tag{7c}$$

where, ∇_S is the gradient operator and $\vec{v}$ is the fluid velocity on the surface.

The second method neglects the unsteady term and surface charge convection [12,14,15,27], so the Eq. (7c) reduces to simpler surface condition, that is, the continuity of the current:

$$[\![\sigma \vec{E}_n]\!] = 0. \tag{7d}$$

The electrohydrodynamic phenomenon arises due to the generated electric stress at the interface. However, the electric forces are essentially exerted on interfacial free charges and charge dipoles rather than on the dielectric fluid. Therefore, the electric body force ($\vec{F}_E$) can be described [35–37] in terms of divergence of the Maxwell stress, $\boldsymbol{\sigma_M} = \varepsilon \vec{E}\vec{E} - \frac{\varepsilon}{2}[1 - \frac{\rho}{\varepsilon}(\frac{\partial \varepsilon}{\partial \rho})]E^2\ \boldsymbol{I}$; and $\overrightarrow{F_E}$ coupled with hydrodynamic and surface tension forces drive the EHD flow in a medium of continuously varying permittivity and bulk charges. The electric force ($\overrightarrow{F_E}$) per unit volume, as calculated by taking divergence of the Maxwell stress tensor, becomes

$$\vec{F}_E = \nabla \cdot \overrightarrow{\sigma_M} = q_v \vec{E} - \frac{1}{2}\vec{E} \cdot \vec{E} \nabla \varepsilon + \nabla\left(\frac{1}{2}\vec{E} \cdot \vec{E}\frac{\partial \varepsilon}{\partial \rho}\rho\right). \tag{8}$$

Under the assumption of incompressibility, by inserting electric body force together with surface tension force into the Navier-Stokes equation, one obtains the governing equation [e.g., Eq. (20) in Hua *et al.* [15]] for the EHD flow phenomenon, known as the leaky dielectric model. The relevant boundary conditions at the interfaces are the continuity of the velocity, $\vec{\boldsymbol{u}}_{\text{in}} = \vec{\boldsymbol{u}}_{\text{out}}$, and balancing the jump in total stress and interfacial tension, $[\![\vec{\boldsymbol{n}} \cdot \vec{\boldsymbol{T}}^{H}]\!] = \gamma\kappa\vec{\boldsymbol{n}} - [\![\vec{\boldsymbol{n}} \cdot \vec{\boldsymbol{T}}^{E}]\!]$, where $\kappa = [(I - \vec{\boldsymbol{n}}\,\vec{\boldsymbol{n}}) \cdot \nabla] \cdot \vec{\boldsymbol{n}}$ is the mean curvature of the interface, and $[\![\cdot]\!]$ denotes jump in hydrodynamic ($\vec{\boldsymbol{T}}^{H}$) and electrical ($\vec{\boldsymbol{T}}^{E}$) stresses across the interface. For the present numerical investigation, the suitable lattice Boltzmann (LB) collision operator to model the nonlinear EHD interactions is elaborated in Secs. II C 1 and II C 2.

Notably, over the years the response of an *isolated leaky dielectric drop*, suspended in an immiscible leaky dielectric medium and subjected to uniform electrostatic field, is extensively examined [9–18]. Due to developed interfacial stresses, the drop experiences *prolate* or *oblate* deformation. Torza *et al.* [10] and Baygents *et al.* [26] present the expression for the drop deformation D in terms of the fluid properties as

$$D = \frac{L - B}{L + B} = \frac{9 f_d}{16\left(2 + \sigma_{\text{in}}/\sigma_{\text{out}}\right)^2}\text{Ca}_E \tag{9}$$

$$f_d = \left(\frac{\sigma_{\text{in}}}{\sigma_{\text{out}}}\right)^2 + 1 - 2\frac{\varepsilon_{\text{in}}}{\varepsilon_{\text{out}}} + \frac{3}{5}\left(\frac{\sigma_{\text{in}}}{\sigma_{\text{out}}} - \frac{\varepsilon_{\text{in}}}{\varepsilon_{\text{out}}}\right)\frac{\left(2 + 3\frac{\mu_{\text{in}}}{\mu_{\text{out}}}\right)}{\left(1 + \frac{\mu_{\text{in}}}{\mu_{\text{out}}}\right)}, \tag{10}$$

where L is end-to-end length of a deformed drop measured along the applied electric field, B is the maximum drop width perpendicular to the electric field, and $\text{Ca}_E(=\frac{\varepsilon_{\text{out}} E^2 R}{\gamma})$ is the electric capillary number (the ratio of electric force and surface tension γ). Herein, the subscripts in and out correspond to drop-fluid and bulk fluid properties, f_d is the discriminating function, and R is the initial drop radius. When $f_d > 0$, the drop deforms into *prolate* form, and for $f_d < 0$ the drop assumes the *oblate* shape.

Additionally, for the leaky dielectric drop the systematic vortical or recirculatory flows are generated both inside and outside by virtue of the developed tangential component of the electric stress at the interface. The resulting tangential velocity at the surface is expressed as [26]

$$u_\theta = -\frac{9\left(\frac{\sigma_{\text{in}}}{\sigma_{\text{out}}} - \frac{\varepsilon_{\text{in}}}{\varepsilon_{\text{out}}}\right)}{5\left(1 + \frac{\mu_{\text{in}}}{\mu_{\text{out}}}\right)\left(\frac{\sigma_{\text{in}}}{\sigma_{\text{out}}} + 2\right)^2}\cos\theta\sin\theta, \tag{11}$$

where θ is the angle between the line joining the drop center and the point on the interface, and the direction of applied electric field. From Eq. (11), it becomes clear that two types of near-field circulations can occur, and their senses are determined by the sign of $\sigma_{\text{in}}/\sigma_{\text{out}} - \varepsilon_{\text{in}}/\varepsilon_{\text{out}}$. Furthermore, the interfacial viscous stress imposed by the vortical circulations can promote *prolate* or *oblate* deformation of a leaky dielectric drop.

B. The electrohydrodynamic interaction

In a homogeneous medium, the net force generated around an *isolated drop* under the influence of uniform electrostatic field is zero, and there occurs no motion of the center of mass. However, in a coupled *two-drop system*, the presence of another neighboring leaky dielectric drop disturbs uniform electric field as induced by an individual drop, and the resulting electric field strength for two dielectric drops is larger than that in far field. Thus, a nonzero net force acts on the drop pair in the direction of the electric field gradient. The typical phenomenon is the well-known dielectrophoresis [20]. By employing the so-called point-dipole model Chiesa *et al.* [38] estimate electrostatic interaction

between two suspended drops as the force between two dipoles located at drop centers. The resulting radial (F_r) and tangential (F_t) components of the electric force, as shown in Fig. 1, are expressed as

$$F_r = \frac{12\pi\varepsilon_{\text{out}}E_\infty^2 R^6\beta^2}{d^4}[3(\cos\alpha)^2 - 1], \tag{12}$$

$$F_t = -\frac{12\pi\varepsilon_{\text{out}}E_\infty^2 R^6\beta^2}{d^4}\sin 2\alpha, \tag{13}$$

where d is the center-to-center distance between two drops, α is the angle between the applied electric field and the line joining two drop centers, and β is given by

$$\beta = 1 - 3\Big/\left(\frac{\varepsilon_{\text{in}}}{\varepsilon_{\text{out}}} + 2\right). \tag{14}$$

As mentioned above, two types of vortical circulations can occur due to the applied electric field; sense of which is determined by the sign of $\sigma_{\text{in}}/\sigma_{\text{out}} - \varepsilon_{\text{in}}/\varepsilon_{\text{out}}$. According to Baygents *et al.* [26] at $\alpha = 0^\circ$ the dipolar far field (hydrodynamic or electrical) would create essential vortical outer circulations to enforce a drop pair either move closer or apart; for $\sigma_{\text{in}}/\sigma_{\text{out}} > \varepsilon_{\text{in}}/\varepsilon_{\text{out}}$ the vortical circulations around one drop shall push the second drop away, and for $\sigma_{\text{in}}/\sigma_{\text{out}} < \varepsilon_{\text{in}}/\varepsilon_{\text{out}}$ the circulations around one drop will pull the second drop closer. The postulated EHD interactions [26] can apparently outline drop pair's relative motion. However, virtually no experimental or numerical exploration is available in literature that could help better comprehend the related physics or kinetics that is essentially based on established principles of paired vortex dynamics. Moreover, the presented scenarios like breakup of a droplet upon coalescence remained unknown. A systematic numerical study is conducted here by taking into account full nonlinear effects, widely varied dielectric properties, and aligned and nonaligned electric field, with an objective to unfold precise physical mechanisms that control a drop pair's relative motion, *prolate or oblate* deformation, *coalescence*, and postcoalescence *breakup*.

C. The numerical method and implementation

1. The explicit forcing interparticle-potential Lattice Boltzmann Method

Important to mention at this point that, in the Shan and Chen [33] model the external forces that introduced into the discrete Boltzmann equations through an equilibrium velocity shift bring in some inherent error [39] and produces relaxation time dependent solution for the multiphase flow, leading to creation of large spurious eddies in vicinity of interface. As a remedy, Porter *et al.* [34] recently proposed the explicit forcing LB model wherein the forcing term is directly incorporated into the discrete Boltzmann equation. In the present work, we have implemented below the recent LB model of Porter *et al.* [34], which is substantially improved on various fronts [39,47]. The LB model is expressed as

$$\begin{aligned} &f_l^k(\vec{x} + \vec{e}_l\Delta t,\, t + \Delta t) - f_l^k(\vec{x},\, t) \\ &= -\frac{f_l^k(\vec{x},\, t) - f_l^{k(eq)}\left(n_k, \vec{u}_k^{eq}\right)}{\tau^k} + \Delta t\left(1 - \frac{1}{2\tau^k}\right)\frac{\left(\vec{e}_l - \vec{u}_k^{eq}\right)\cdot\vec{F}_k}{\rho_k c_s^2}\, f_l^{k(eq)}\left(n_k, \vec{u}_k^{eq}\right), \end{aligned} \tag{15}$$

where, $f_l^k(\vec{x},\, t)$ is the probability distribution function of the kth component in the direction of lth molecular velocity ($\overrightarrow{e_l}$) at a position $\vec{x}$ at time t, and τ_k is the nondimensional relaxation time. Herein, as evidenced below, the adopted D2Q9 [34,40] model efficiently and accurately predicts the multiphase flow interactions. The $f_l^{k(eq)}(n_k, \vec{u}_k^{eq})$, representing local Maxwellian equilibrium

distribution, is given by [13,34,40,41]

$$
\begin{aligned}
f_0^{k(eq)} &= \alpha_k n_k - \frac{2}{3} n_k \vec{u}_k^{eq} \cdot \vec{u}_k^{eq}, \\
f_l^{k(eq)} &= \frac{(1-\alpha_k) n_k}{5} + \frac{1}{3} n_k \left(\overrightarrow{e_l} \cdot \vec{u}_k^{eq}\right) + \frac{1}{2} n_k \left(\overrightarrow{e_l} \cdot \vec{u}_k^{eq}\right)^2 - \frac{1}{6} n_k \vec{u}_k^{eq} \cdot \vec{u}_k^{eq} \quad \text{for } l = 1\text{–}4, \\
f_l^{k(eq)} &= \frac{(1-\alpha_k) n_k}{20} + \frac{1}{12} n_k \left(\overrightarrow{e_l} \cdot \vec{u}_k^{eq}\right) + \frac{1}{8} n_k \left(\overrightarrow{e_l} \cdot \vec{u}_k^{eq}\right)^2 - \frac{1}{24} n_k \vec{u}_k^{eq} \cdot \vec{u}_k^{eq} \quad \text{for } l = 5\text{–}8.
\end{aligned} \tag{16}
$$

The discrete molecular velocity $\overrightarrow{e_l}$ is expressed as

$$
\overrightarrow{e_l} = \begin{Bmatrix} \vec{0}, & l = 0, \\ \left[\cos\frac{(l-1)\pi}{2},\ \sin\frac{(l-1)\pi}{2}\right], & l = 1\text{–}4, \\ \sqrt{2}\left\{\cos\left[\frac{(l-5)\pi}{2} + \frac{\pi}{4}\right],\ \sin\left[\frac{(l-5)\pi}{2} + \frac{\pi}{4}\right]\right\}, & l = 5\text{–}8 \end{Bmatrix}. \tag{17}
$$

In Eqs. (16), the parameter α_k is related to the speed of sound in the D2Q9 [40] model and is given by $(c_s^k)^2 = 0.6(1-\alpha_k)$. n_k is the total number of density of the kth component, defined by $n_k = \sum_l f_l^k$. The mass density of the kth component is $\rho_k = m_k n_k = m_k \sum_l f_l^k$; where m_k is the kth molecular mass. The kth component of fluid velocity $\vec{u}_k^{eq}$ at the equilibrium state is determined by

$$
\vec{u}_k^{eq} = \left(\sum_{k=0}^{s} \frac{\rho_k \vec{u}_k}{\tau_k}\right) \Big/ \left(\sum_{k=0}^{s} \frac{\rho_k}{\tau_k}\right), \tag{18}
$$

$$
\rho_k \vec{u}_k = \sum_l f_l^k \vec{e}_l + 0.5 \Delta t\ \vec{F}_k, \tag{19}
$$

where $S+1$ represents total number of components in the multiphase system, $\vec{F}_k$ is total force acting on kth component, including fluid-fluid interaction ($\vec{F}_k^{\text{int}}$) and electric ($\vec{F}_k^{\text{ele}}$) forces, as appropriate for this work.

In the interparticle potential model, the interactive force between particles of the kth component at location $\vec{x}$ and the $\bar{k}$th component at the location $\vec{x}'$ is assumed to be proportional to product of the effective number density $\varphi_k(n_k)$, which is defined as a function of local number density [34,40]. Following past investigations [13,40,42], $\varphi_k(n_k)$ is chosen here as n_k. Thus, the total interaction force acting on the kth component at $\vec{x}$ is given by

$$
\overrightarrow{F}_k^{\text{int}}(\vec{x}) = -n_k(\vec{x}) \sum_{x'} \sum_{\bar{k}} G_{k\bar{k}}(\vec{x},\vec{x}')\, n_{\bar{k}}(\vec{x}')\, (\vec{x} - \vec{x}'). \tag{20}
$$

Here $G_{k\bar{k}}(\vec{x},\vec{x}')$ is the Green's function that satisfies $G_{k\bar{k}}(\vec{x},\vec{x}') = G_{\bar{k}k}(\vec{x},\vec{x}')$ and the magnitude of which controls the strength ($g_{k\bar{k}}$) of the interaction potential. For the D2Q9 lattice arrangement, we adopt a method similar to that proposed by Marty and Chen [43] to obtain the required interaction potential, by projecting the four-dimensional face-centered hypercubic (4D FCHC) lattices to the present D2Q9 format. Consequently, the potential that couples nearest and next nearest neighbors becomes

$$
G_{k\bar{k}}(\vec{x},\vec{x}') = \begin{Bmatrix} g_{k\bar{k}}, & |\vec{x} - \vec{x}'| = 1 \\ \frac{g_{k\bar{k}}}{4}, & |\vec{x} - \vec{x}'| = \sqrt{2} \\ 0, & \text{otherwise} \end{Bmatrix}. \tag{21}
$$

The whole fluid velocity ($\vec{u}$) is thereby expressed in the following form:

$$\vec{u} = \frac{\sum_k \rho_k \vec{u}_k}{\sum_k \rho_k}. \tag{22}$$

And the kinematic fluid viscosity is expressed as

$$\upsilon = \frac{1}{3}\sum_k \frac{\rho_k \tau_k}{\rho} - \frac{1}{6}. \tag{23}$$

Accordingly, for the kth component, the viscosity is reduced to

$$\upsilon = \tfrac{1}{3}\tau_k - \tfrac{1}{6}. \tag{24}$$

2. The LBM approach for computing the electric field and treatment of interface

In principle, the governing electric potential equation [Eq. (7)] is an elliptic equation, while LBM is a method that essentially solves parabolic equation. Thus, the solution of Eq. (7) is conveniently obtained (e.g., He and Li [44]; Guo *et al.* [45]) as the steady solution of the following equation [Eq. (25)] in the LBM timescale:

$$\frac{\partial V}{\partial t} + \nabla \cdot (\sigma \nabla V) = 0. \tag{25}$$

For this, the new particle distribution function h_l is introduced [44,45] and expressed as

$$h_l(\vec{x} + \vec{e}_l \Delta t,\, t + \Delta t) - h_l(\vec{x},\, t) = -\frac{h_l(\vec{x},\, t) \;-\; h_l^{eq}(\vec{x},\, t)}{\tau^h}. \tag{26}$$

The corresponding equilibrium distributions h_l^{eq} and the relaxation time τ_h are expressed as

$$\begin{aligned} h_0^{eq} &= \tfrac{4}{9}V, \\ h_l^{eq} &= \tfrac{1}{9}V, \quad l = 1\text{–}4, \\ h_l^{eq} &= \tfrac{1}{36}V, \quad l = 5\text{–}8, \end{aligned} \tag{27a}$$

$$\tau_h = 3\sigma + 0.5, \tag{27b}$$

where σ represents a combination of electric conductivities, as described below. Based on Eqs. (26) and (27), Eq. (25) can be recovered using Chapman-Enskog expansion [46], while electric potential V is defined as

$$V = \sum_l h_l. \tag{28}$$

Notably, the influence of the electric field in the EHD motion activates through the Maxwell's stress that is developed due to different fluid conductivity and permittivity and/or electric field strength. In numerical algorithms solving the two-phase hydrodynamics (e.g., Kang *et al.* [42,47]), the sharp interface is often treaded as a diffused one, spanning over a thin region (of three grid size [14,42]) wherein physical properties continuously and smoothly transit from a value of one phase to that of another phase. Therefore, the electric force existing on the interface is induced by the nonuniform dielectric properties (σ and ε). Here we employ the following interpolation process to calculate the electric field properties:

$$\begin{aligned} \rho\varepsilon &= \varepsilon_{\text{in}}\rho_{\text{in}} + \varepsilon_{\text{out}}\rho_{out}\ , \\ \rho\sigma &= \sigma_{\text{in}}\rho_{\text{in}} + \sigma_{\text{out}}\rho_{out}\ , \end{aligned} \tag{29}$$

where $\rho(=\rho_{\text{in}} + \rho_{\text{out}})$ denotes total density for the mixture. For clarity, the computed variations of ρ_{in}, ρ_{out} , ε, across a drop interface, the invariances of the flow interaction and the resulting interfacial

TABLE I. The computed deformation rate D of a drop for implemented various domain sizes; $\mathrm{Ca}_E = 0.18$, $\varepsilon_{\mathrm{in}}/\varepsilon_{\mathrm{out}} = 10$, and $\sigma_{\mathrm{in}}/\sigma_{\mathrm{out}} = 1.81$.

Domain size/lattices	128×128	256×256		300×300	
Radius	14	14	11	14	16
D (deformation rate)	0.162	0.1632	0.1634	0.16325	0.1631

tangential electric stress upon using Eq. (29) and a proposed new formula [Eq. (A1)] are elucidated in Appendix A.

In addition, for dealing with two different fluids, the electric force $\vec{F}_k^{\mathrm{ele}}$ obtained from the Maxwell's stress needs to be separated into two parts and suitably applied for each set of fluid properties. In a way consistent to Eq. (29), we divide this force according to density ratio as

$$\vec{F}_k^{\mathrm{ele}} = \frac{\rho_k}{\rho}\vec{F}_E, \quad k = 1,2. \tag{30}$$

Note however that, the condition of isotropy [34] is broadly imposed while calculating the $\overrightarrow{F_E}$.

III. RESULTS AND DISCUSSION

Before presenting detailed simulated results, first, effect of the computational domain size is examined to employ an appropriate flow configuration and avoid any unphysical influence. Table I presents computed deformation rate D of a drop using different lattice sizes and $\mathrm{Ca}_E = 0.18$, $\varepsilon_{\mathrm{in}}/\varepsilon_{\mathrm{out}} = 10$, $\sigma_{\mathrm{in}}/\sigma_{\mathrm{out}} = 1.81$. Notably, Table I shows that lattice numbers greater or equal to 256×256 are sufficiently large to generate the domain size-independent numerical results. Second, the computed D at $\mathrm{Ca}_E = 0.18$, $\varepsilon_{\mathrm{in}}/\varepsilon_{\mathrm{out}} = 10$, $\sigma_{\mathrm{in}}/\sigma_{\mathrm{out}} = 1.81$, for three different drop radii, as presented in Table I, reveals that D remains virtually unchanged when the domain is covered by 300×300 lattices. Accordingly simulations are carried out in two dimensions in a domain covered by 300×300 D2Q9 lattices with implemented periodic conditions for fluid motion in both directions (Fig. 1) and the Neumann-type spanwise boundary condition ($\partial V/\partial y = 0$) for the electric potential. In the first part of the study (Sec. III C), two leaky dielectric drops are symmetrically placed at $\alpha = 0^\circ$ in a domain filled with another immiscible leaky dielectric fluid. The system remains exposed to the uniform electric field that is generated by maintaining the (constant) higher and lower electric potential at left (V_+) and right (V_-) boundaries of the domain. The molecular mass (m_k) is set to be 1.0. To examine the influence of the electric field on the drop-drop response, the densities of the drop fluid and the surrounding fluid are assumed to be identical. It may be noted from Eqs. (9)–(11), the drop deformation (D) and interface velocity (u_θ) are weak functions of fluid viscosity. Therefore, the viscosity ratio was fixed to be 1.0 (i.e., $\mu_{\mathrm{in}}/\mu_{\mathrm{out}} = 1$). Additionally, in the adopted explicit forcing LBM formulation [34] the interaction potential strengths are appropriately selected as $g_{12} = g_{21} = 0.275$, $g_{11} = g_{22} = 0.0$, and the relaxation time τ_k is chosen as 1.0. Moreover, in Appendix B we describe how the present explicit forcing LB model [34] drastically reduces the spurious currents [39] in a drop with respect to the Shan and Chen [33] model.

A. Computation of surface tension

Now, the bubble test [42] is performed to calculate surface tension γ of a drop suspended in another fluid, which also helps to validate the adopted LB approach. For this, in the absence of electric field, a circular drop (of radius R) of one fluid is placed symmetrically in a (2D) domain filled with a second fluid. At equilibrium, the pressure jump ($p_{\mathrm{in}} - p_{\mathrm{out}}$) created across the drop interface (in absence of body force) is balanced by the surface tension γ. The evolution of the drop

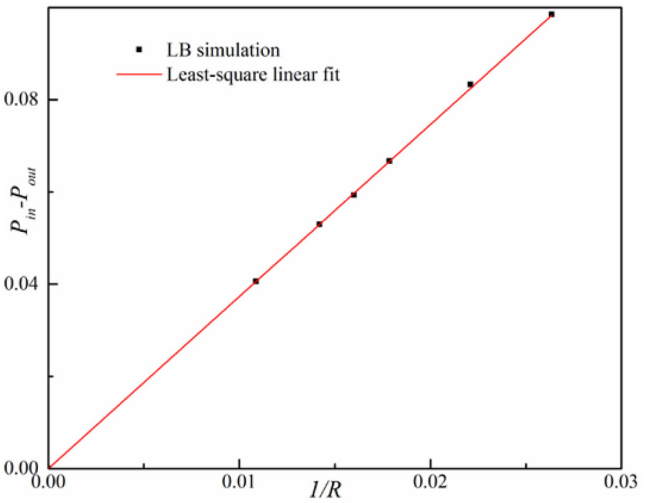

FIG. 2. Computation of surface tension for a single drop through Laplace's law. The slope (surface tension) is 0.268.

is governed [48] by the Laplace's law,

$$p_{\text{in}} - p_{\text{out}} = \gamma/R, \tag{31}$$

and the pressure p for the whole fluid is expressed as [40]

$$p = \frac{1}{3}\sum_{k} n_k + \frac{3}{2}\sum_{k\bar{k}} g_{k\bar{k}} n_k n_{\bar{k}}. \tag{32}$$

In a 300×300 lattice structure, the initial density for component 1 was set as 2.0 in the drop and 0.01 for outer fluid; whereas the density for component 2 was initially set to be 0.01 for the drop and 2.0 elsewhere. Simulations for the multicomponent fluid flow with different component densities are then conducted with various R, and the resulting pressure difference $p_{\text{in}} - p_{\text{out}}$ is computed at the steady state. Since LBE is a dynamical procedure, the static state for the drop is achieved through time evolution of about 15 000 time steps. Figure 2 presents the computed $p_{\text{in}} - p_{\text{out}}$ for varied R, together with the fitted solid line that obeys the Laplace equation [Eq. (31)]. Notably, the computed slope, that is, the surface tension becomes $\gamma = 0.268$. The observed linear fit (in Fig. 2) between computed $p_{\text{in}} - p_{\text{out}}$ and $1/R$ is clearly consistent with the Laplace equation.

B. The validation of the explicit forcing LBM model for computing EHD drop deformation

In this section, first, the EHD behavior of a *single leaky dielectric drop* suspended in another leaky dielectric fluid and subjected under an applied electric field is numerically studied using the LBM approach. In recent years the leaky model is broadly used [12,15,49] to predict small drop deformation. Extensive simulations are performed here for varied electric capillary number (Ca_E), conductivity ratio ($\sigma_{\text{in}}/\sigma_{\text{out}}$), and permittivity ratio ($\varepsilon_{\text{in}}/\varepsilon_{\text{out}}$) to examine the physical transformation of a single drop and demonstrate efficiency and accuracy of the adopted numerical methodology in correctly predicting the EHD interaction. For the simulated flows, following Feng and Scott [49], the Reynolds number Re is calculated or reported based on the maximum interface velocity $u = \frac{9R\,\varepsilon_{\text{in}}E_\infty^2}{10\,\mu_{\text{in}}}\,[|\frac{\varepsilon_{\text{out}}}{\varepsilon_{\text{in}}}\,\frac{\sigma_{\text{in}}}{\sigma_{\text{out}}} - 1|/(2 + \frac{\sigma_{\text{in}}}{\sigma_{\text{out}}})^2(1 + \frac{\mu_{\text{out}}}{\mu_{\text{in}}})]$ and the drop radius R.

Figure 3(a) presents our computed results of (single) drop deformation D for varied Ca_E (up to onset of breakup), together with available theoretical or numerical results [12,50]. First, for the case [12] of the simulated *oblate* deformation at $\sigma_{\text{in}}/\sigma_{\text{out}} = 0.1$, $\varepsilon_{\text{in}}/\varepsilon_{\text{out}} = 2.0$, $\text{Ca}_E \leqslant 0.32$,

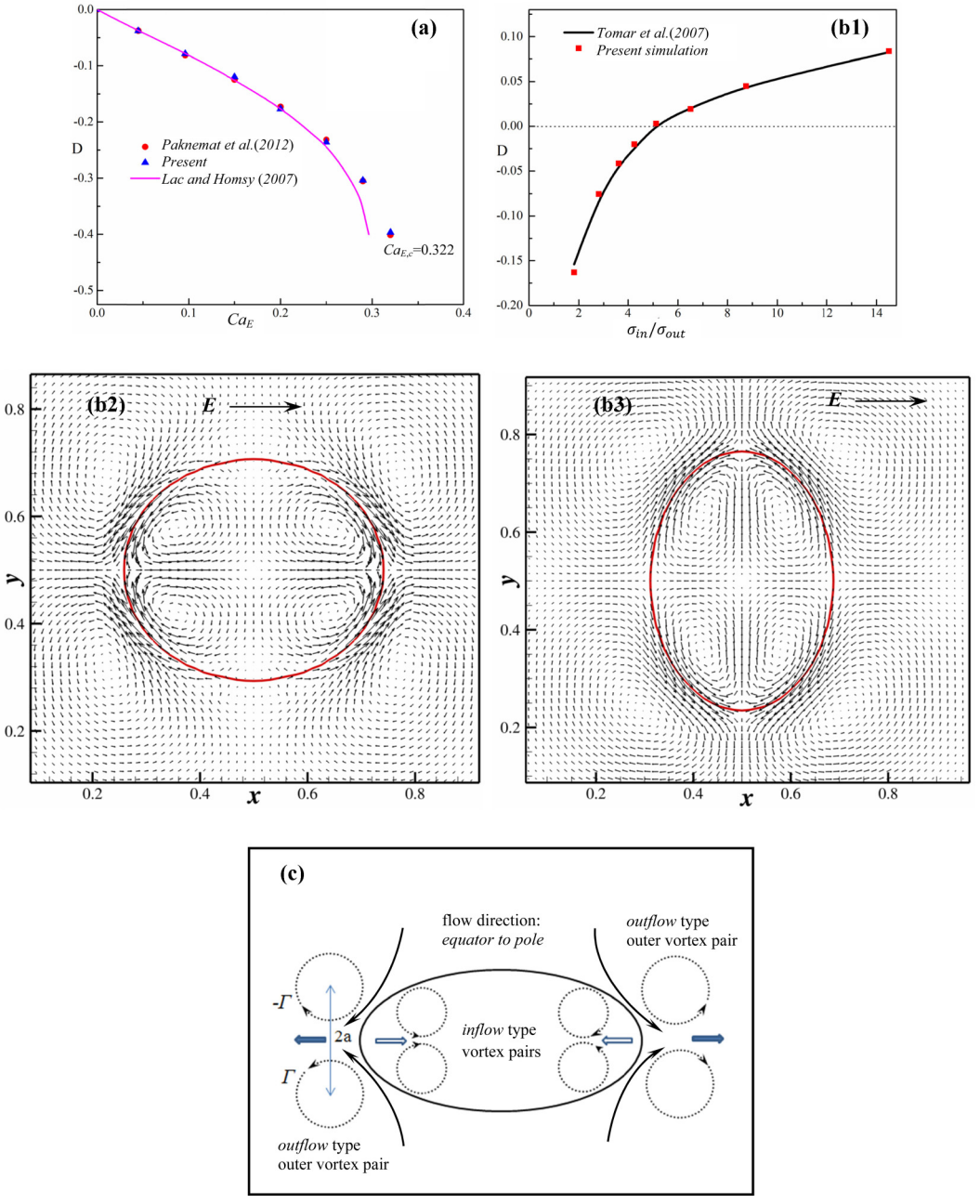

FIG. 3. (a) Computed effect of the electric capillary number (Ca_E) on the deformation rate D of a drop and comparison between present result and available numerical predictions [12,50] for $\sigma_{in}/\sigma_{out} = 0.1$, $\varepsilon_{in}/\varepsilon_{out} = 2.0$, $0.54 \leqslant Re \leqslant 4.09$; (b1) simulated variation of D with σ_{in}/σ_{out} and comparison with existing numerical results [14] at $\varepsilon_{in}/\varepsilon_{out} = 10.0, Ca_E = 0.18$; (b2) the computed *prolate* drop deformation (red solid curve is the interface) and electrically induced velocity field at $\sigma_{in}/\sigma_{out} = 14.5$, $\varepsilon_{in}/\varepsilon_{out} = 10.0$, $Ca_E = 0.18$; (b3) computed *oblate* drop deformation and induced velocity at $\sigma_{in}/\sigma_{out} = 1.81$, $\varepsilon_{in}/\varepsilon_{out} = 10.0$, $Ca_E = 0.18$; (c) sketches of locally grown *inflow*- and *outflow*-type vortex pairs and induced influences.

Fig. 3(a) shows that for small D the present results agree very well with the results of Lac and Homsy [12]. However, for larger deformation the observed deviation occurs possibly because of relatively higher Re ($0.54 \leqslant \mathrm{Re} \leqslant 4.09$) used in the present nonlinear model and assumed 2D character of the flow interaction; whereas Lac and Homsy [12] studied the axisymmetric case under creeping condition. On the other hand, our simulated D [Fig. 3(a)] appears quite similar to the 2D nonlinear solution of Paknemat *et al.* [50], obtained *via* level set method. Notably, as Ca_E exceeds certain critical value, the droplet exhibits breaking behavior [12,50]. The critical electric capillary number ($\mathrm{Ca}_{E,c}$) that facilitates onset of breakup is computed here by minutely varying Ca_E; and our predicted $\mathrm{Ca}_{E,c} = 0.322$ compares closely with the value $\mathrm{Ca}_{E,c1} = 0.297$ obtained by Lac and Homsy [12] (using BEM), and with $\mathrm{Ca}_{E,c2} = 0.321$ of Paknemat *et al.* [50]. The noted relatively early breakup [12] of an axisymmetric drop in Stokes regime can be influenced by transverse shear or curvature. For further clarity, Fig. 3(b1) displays our computed D and numerical results of Tomar *et al.* [14] for increased $\sigma_{\mathrm{in}}/\sigma_{\mathrm{out}}$ over 1.81 to 14.5, while $\varepsilon_{\mathrm{in}}/\varepsilon_{\mathrm{out}} = 10.0$, $\mathrm{Ca}_E = 0.18$ kept fixed. It shows, the present results virtually coincide with those of Tomar *et al.* [14]. Moreover, as drops of varied $\sigma_{\mathrm{in}}/\sigma_{\mathrm{out}}$ changed shape, Figs. 3(b2) and 3(b3) captures computed physical transformation of a drop in the range $1.81 \leqslant \sigma_{\mathrm{in}}/\sigma_{\mathrm{out}} \leqslant 14.5$, while $\varepsilon_{\mathrm{in}}/\varepsilon_{\mathrm{out}} = 10.0$, $\mathrm{Ca}_E = 0.18$ kept fixed. Note that, the drop transforms from *prolate* [Fig. 3(b2); $\sigma_{\mathrm{in}}/\sigma_{\mathrm{out}} = 14.5$] to *oblate* shape [Fig. 3(b3); $\sigma_{\mathrm{in}}/\sigma_{\mathrm{out}} = 1.81$] for gradually decreased $\sigma_{\mathrm{in}}/\sigma_{\mathrm{out}}$. The discriminating function f_d [Eq. (10)] which depends on fluid properties is known to determine [10,26] the axial drop deformation, and our results [Figs. 3(b2) and 3(b3)] clearly follow the stated analytical condition. In addition, Figs. 3(b2) and 3(b3) reveal that besides shape change, the sense of internal kinetics or vortices in a drop is clearly dependent on the sign of $\sigma_{\mathrm{in}}/\sigma_{\mathrm{out}} - \varepsilon_{\mathrm{in}}/\varepsilon_{\mathrm{out}}$. Note that, for $\sigma_{\mathrm{in}}/\sigma_{\mathrm{out}} > \varepsilon_{\mathrm{in}}/\varepsilon_{\mathrm{out}}$ the circulation in first quadrant is clockwise [Fig. 3(b2); $\sigma_{\mathrm{in}}/\sigma_{\mathrm{out}} = 14.5$, $\varepsilon_{\mathrm{in}}/\varepsilon_{\mathrm{out}} = 10.0$], and for $\sigma_{\mathrm{in}}/\sigma_{\mathrm{out}} < \varepsilon_{\mathrm{in}}/\varepsilon_{\mathrm{out}}$ the said circulation [Fig. 3(b3); $\sigma_{\mathrm{in}}/\sigma_{\mathrm{out}} = 1.81$, $\varepsilon_{\mathrm{in}}/\varepsilon_{\mathrm{out}} = 10.0$] nature is distinctly reversed. *The important fact to note* in Figs. 3(b2) and 3(b3) that, irrespective of *prolate or oblate* shapes, drops inevitably appear elongated along the direction of the dominant *outflow*-natured or outward-moving near-interface *outer vortex pairs* that formed at their major-axis ends. On the other hand, presented consistent variations (Fig. 3) of our simulated results with existing findings [12,14,50] demonstrate that the adopted explicit forcing LBM method can correctly predict the EHD flow physics of suspended drops. For clear understanding, a sketch showing *outflow*-type outward (horizontal) motion of two outer vortex pairs and the induced *prolate* deformation of a drop is presented in Fig. 3(c).

C. EHD interaction of drop pairs at $\alpha = 0°$

For the leaky dielectric drop pair [Fig. 4(a)] aligned along the direction of an applied electric field ($\alpha = 0^\circ$), the mutual interaction is driven by two distinct mechanisms. (i) The electric interaction by induced electric field [Eqs. (12)–(14)] which develops in the presence of the second drop in vicinity and creates local imbalance, helping generation of a far-field dipole that tends to drive two drops closer. (ii) The electrically driven hydrodynamic interaction owing to bulk fluid circulation produced [see Eq. (11)] *via* the interfacial stretching and dynamics of drops, that is capable of inducing attractive or repulsive forces between a drop pair (depending on sign of $\sigma_{\mathrm{in}}/\sigma_{\mathrm{out}} - \varepsilon_{\mathrm{in}}/\varepsilon_{\mathrm{out}}$) as discussed in Sec. II B. From Eqs. (11)–(14) it becomes clear that the *permittivity contrast* $\varepsilon_{\mathrm{in}}/\varepsilon_{\mathrm{out}}$ can be a sensitive factor for effectively manipulating the above said two physical mechanisms or interactions. Guided by such an intuition, and to provide clear understanding of diverse drop-drop or drop-fluid interactions and related physics, the systematically planned simulations are performed here using full nonlinear set of equations. For the sake of clarity (and displaying essential validity of the LB approach) at this point we compute the tangential electric stress that developed along the interface of the left-side drop, as drop pair was placed in the electric field. For a test case of $d_0/R = 2.2$, $\varepsilon_{\mathrm{in}}/\varepsilon_{\mathrm{out}} = 1.0$, $\sigma_{\mathrm{in}}/\sigma_{\mathrm{out}} = 10$, Fig. 4(b) presents a comparison of our simulated results with the theoretical solution of Sozou [51] and BEM solution of Baygents *et al.* [26]. It is worthy to note that, in Sozou's study [51] two restrictions were present. First, no relative motion occurs

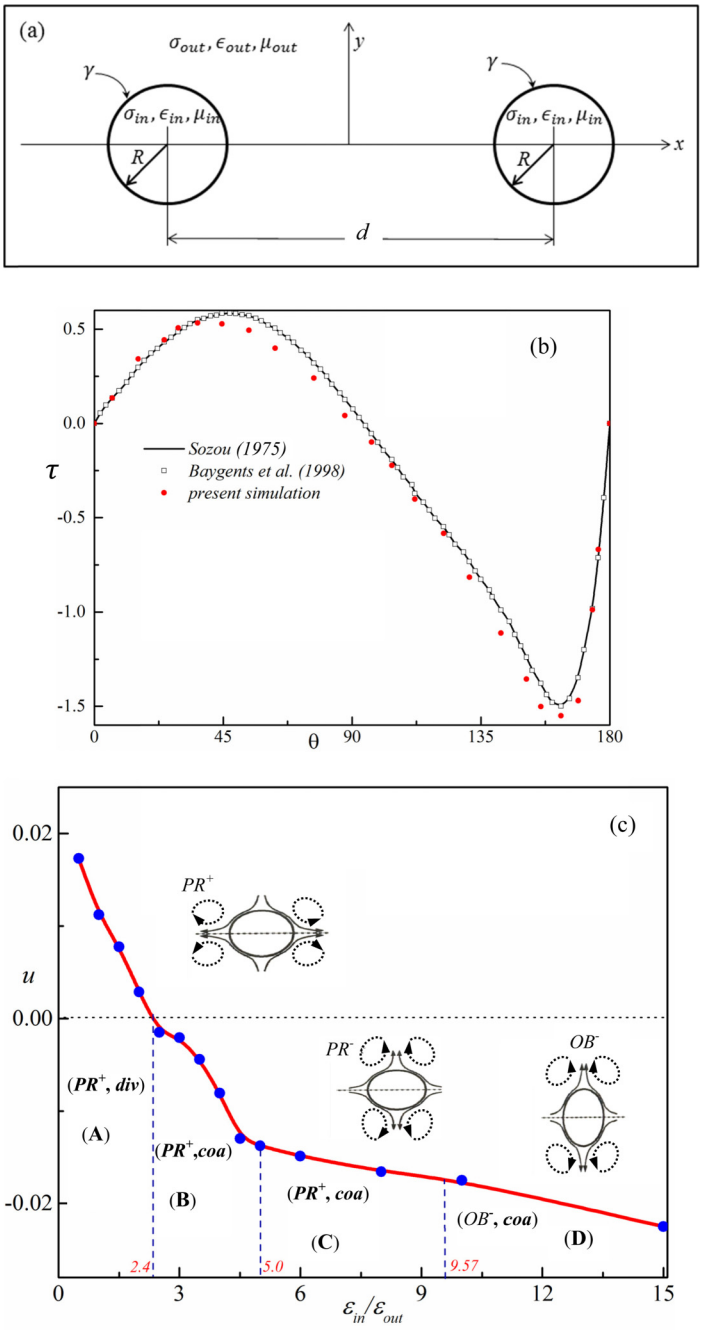

FIG. 4. (a) A sketch of two identical liquid drops aligned with the direction of the applied electric field. (b) The computed tangential electric stress (τ) along the interface of the left-side droplet for $d_0/R = 2.2$, $\varepsilon_{\rm in}/\varepsilon_{\rm out} = 1.0$, $\sigma_{\rm in}/\sigma_{\rm out} = 10$, and comparison with Stokes solution of Baygents *et al.* [26] and Sozou [51]. (c) The computed drop velocity (u) with varied permittivity ratio ($\varepsilon_{\rm in}/\varepsilon_{\rm out}$) at fixed $\sigma_{\rm in}/\sigma_{\rm out} = 5.0$, $\mathrm{Ca}_E = 0.46$. The positive u values represent divergence of two drops, while negative u shows two drops move closer. *PR* denotes *prolate*, *OB* denotes *oblate* shape; exponents $+/-$ denote two *outflow*-type outer vortex pairs induced *equator to pole* and *pole to equator* flow directions, as shown in insets; *div* denotes divergence of two drops, and *coa* denotes coalescence of two drops.

between two equivalent creeping drops, and second, the drops retain the spherical shape. In our study, we relax these constraints and take into account the influence of advection; demonstrating that due to droplet deformation and relative motion the location of the maximum tangential electric stress moves leftward [Fig. 4(b)] on the left half, and persisting relatively stronger tangential electric stress for $\theta > 90^\circ$ results owing to development of higher local curvature on the leading face. However, while being closely consistent to reported [26,51] linear theory, the presented results in Fig. 4(b) further exhibit the suitability of the adopted method in correctly simulating EHD interactions. Now we focus on exploring detailed physics that lead to electrohydrodynamic interaction or coalescence for a drop pair at $\alpha = 0^\circ$.

Figure 4(c) presents the important *characteristic signatures of coupled drop-drop motion* under widely varied $0.25 \leqslant \varepsilon_{\text{in}}/\varepsilon_{\text{out}} \leqslant 20.0$, when $\sigma_{\text{in}}/\sigma_{\text{out}} = 5.0, \text{Ca}_E = 0.46$ kept fixed, and initial center-to-center separation of the drops [Fig. 4(a)] is set to $d = 4R$. The characteristic drop velocity u at a particular $\varepsilon_{\text{in}}/\varepsilon_{\text{out}}$ is calculated following the relative motion of drop centroids over a specified time interval Δt, and the sign of u, *negative* or *positive*, is decided depending on whether the drops move closer or apart. As Fig. 4(c) shows, a drop pair experiences *four distinct classes of movement or deformation mechanisms* over stretches: (i) A ($0.25 \leqslant \varepsilon_{\text{in}}/\varepsilon_{\text{out}} < 2.4$; divergence as the PR^+ drop pair), (ii) B ($2.4 < \varepsilon_{\text{in}}/\varepsilon_{\text{out}} < 5.0$; coalescence as the PR^+ drop pair), (iii) C ($5.0 < \varepsilon_{\text{in}}/\varepsilon_{\text{out}} < 9.57$; coalescence as PR^- drop pair), and (iv) D ($\varepsilon_{\text{in}}/\varepsilon_{\text{out}} > 9.57$; coalescence in the OB^- form, and subsequent breakup in a direction orthogonal to applied electric field), for varied $\varepsilon_{\text{in}}/\varepsilon_{\text{out}}$.

1. Relative motion and prolate departure or coalescence in stretches A, B, and C

Equations (12)–(14) reveal, at $\alpha = 0^\circ$ only the radial component F_r of electric force exists. However, for increased $\varepsilon_{\text{in}}/\varepsilon_{\text{out}}$ the radial force F_r increases, that influences a drop pair to move closer. Additionally, Eq. (11) shows, the variation of $\varepsilon_{\text{in}}/\varepsilon_{\text{out}}$, in addition to changing the sign of $\sigma_{\text{in}}/\sigma_{\text{out}} - \varepsilon_{\text{in}}/\varepsilon_{\text{out}}$, also alters the magnitude of the interfacial velocity u_θ on which the strength of the bulk flow depends. First, for the stretch A [Fig. 4(c)] a smaller $\varepsilon_{\text{in}}/\varepsilon_{\text{out}}$ (<2.4) weakens the attractive-natured electric force F_r [Eqs. (12) and (14)] that could have otherwise facilitated the drop pair's coalescence. The second important fact to note from Eq. (11) that, a smaller $\varepsilon_{\text{in}}/\varepsilon_{\text{out}}$ in A creates a stronger bulk flow; and the resulting vortex dynamics-induced forcing, as clearly evidenced below, is responsible for decisively dictating the drop pair move ($u > 0$) apart. Moreover, $\sigma_{\text{in}}/\sigma_{\text{out}} - \varepsilon_{\text{in}}/\varepsilon_{\text{out}} > 0$ over the stretch A. Accordingly throughout A the electrically driven (repulsive) hydrodynamic interaction dominates over (attractive) electric interaction to dictate the drop pair's diverging motion [see $u > 0$ in A; Fig. 4(c)].

To gain clearer insight, in Figs. 5(a1) and 5(a2) we now present transient drop deformation or divergence mechanisms and associated EHD flow phenomena at $\varepsilon_{\text{in}}/\varepsilon_{\text{out}} = 1.0$ that correspond to stretch A [Fig. 4(c)]. Note that, as Fig. 5(a1) reveals, two drops (at $\varepsilon_{\text{in}}/\varepsilon_{\text{out}} = 1.0$) deform *prolately* while moving apart; in clear agreement with existing linear theory [26], when $f_d > 0$ [Eq. (10)]. Figure 5(a2) unfolds the precise induced vortical kinetics, covering both outer as well as inner regions around the drop pair at $t = 1.8T$ (where T denotes 500 lattice unit time). Notably, *inside the drops*, in terms of the left-right distribution, two dominantly *asymmetric* vortex pairs are formed. For the left drop, the left-side (with respect to vertical line of symmetry) inner vortex pair induces a hydrodynamic force that tends to drive the (left) drop or enclosed mass rightward. In contrary, the right-side (inner) vortex pair through their induced velocity tries to push the left drop or enclosed mass leftward. As the relative length of vectors clearly reveal, the strength of the right-side vortex pair is higher than that of vortex pair situated in the left half (which followed for increasing t, as the left-side *inner vortex pair* appeared gradually weaker while the right-side *inner vortex pair* became stronger); and therefore the *net vortex-induced inner thrust on the left drop is directed leftward*. It is important to note that, *just outside* the left drop the counter rotating two pairs of dominant (outer) vortices are formed (evolving symmetrically with respect to major axis) *near left and right edges* [as sketched in Fig. 3(c)], owing to electrically induced bulk fluid motion. Clearly, the stronger outer vortex pair formed at the left

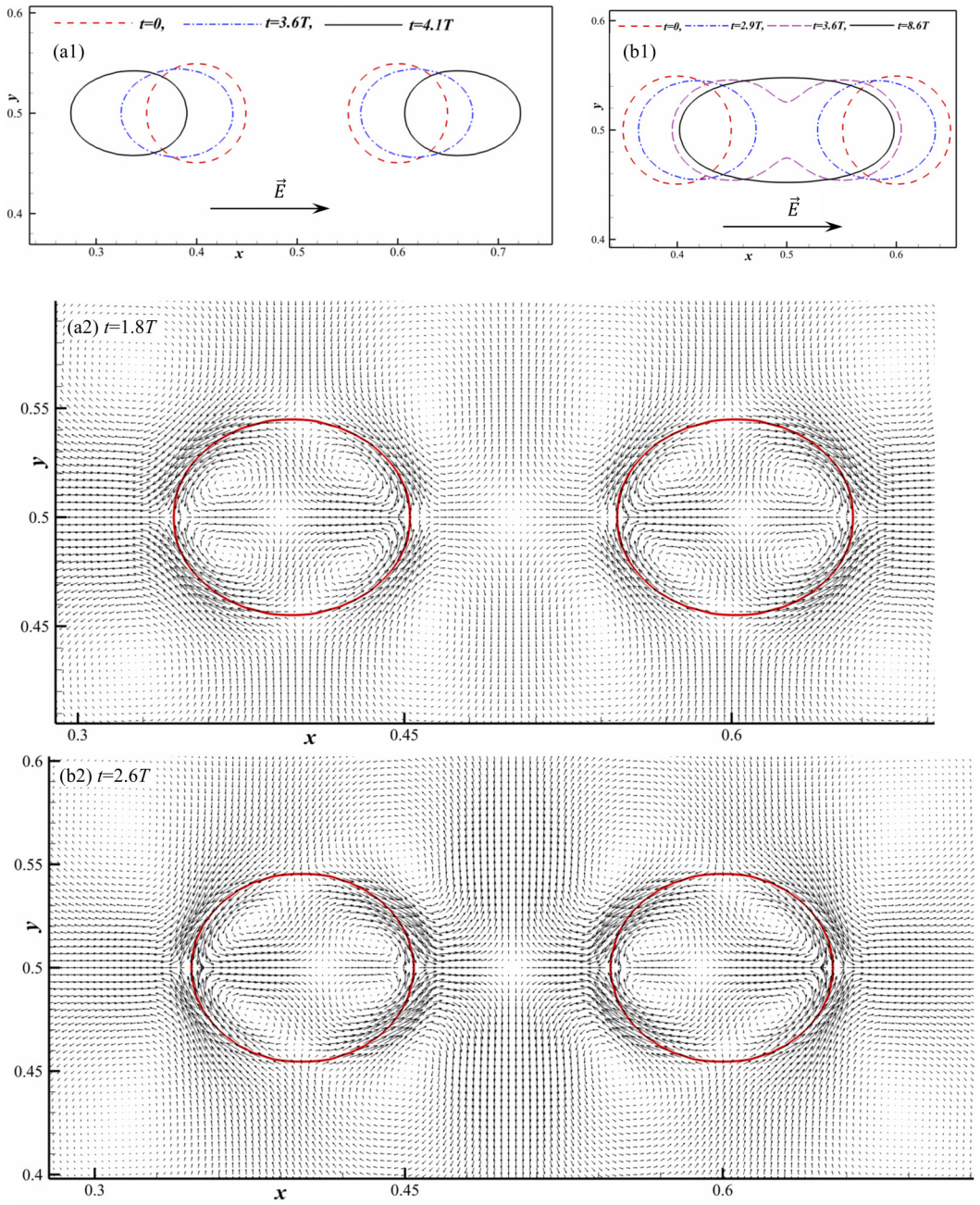

FIG. 5. Simulated *prolate* deformation and relative motion of a drop pair for increased permittivity ratio over $0.5 < \varepsilon_{in}/\varepsilon_{out} \leqslant 9.57$, at fixed $\sigma_{in}/\sigma_{out} = 5.0$, $Ca_E = 0.46$, $\alpha = 0^\circ$. (a1) The transient *divergence* of a drop pair at $\varepsilon_{in}/\varepsilon_{out} = 1.0$ [within stretch A, $\varepsilon_{in}/\varepsilon_{out} < (\varepsilon_{in}/\varepsilon_{out})_{crit1} = 2.4$], and (a2) induced velocity field at $t = 1.8T$; Re = 1.14. (b1) The transient *electrocoalescence* of a drop pair at $\varepsilon_{in}/\varepsilon_{out} = 2.5$, detected in the stretch $B[(\varepsilon_{in}/\varepsilon_{out})_{crit1} = 2.4 < \varepsilon_{in}/\varepsilon_{out} < 5.0 = (\varepsilon_{in}/\varepsilon_{out})_{crit2}]$, and (b2) induced velocity field at $t = 2.6T$; Re = 0.71. (c1) The transitional *coalescence* of a drop pair at $\varepsilon_{in}/\varepsilon_{out} = 7.0$ [within stretch C, $(\varepsilon_{in}/\varepsilon_{out})_{crit2} = 5.0 < \varepsilon_{in}/\varepsilon_{out} < 9.57 = (\varepsilon_{in}/\varepsilon_{out})_{crit3}$], and (c2) the evolution of the surrounding velocity field showing the 90° switching of *outflow*-natured two outer vortex pairs; Re = 0.57.

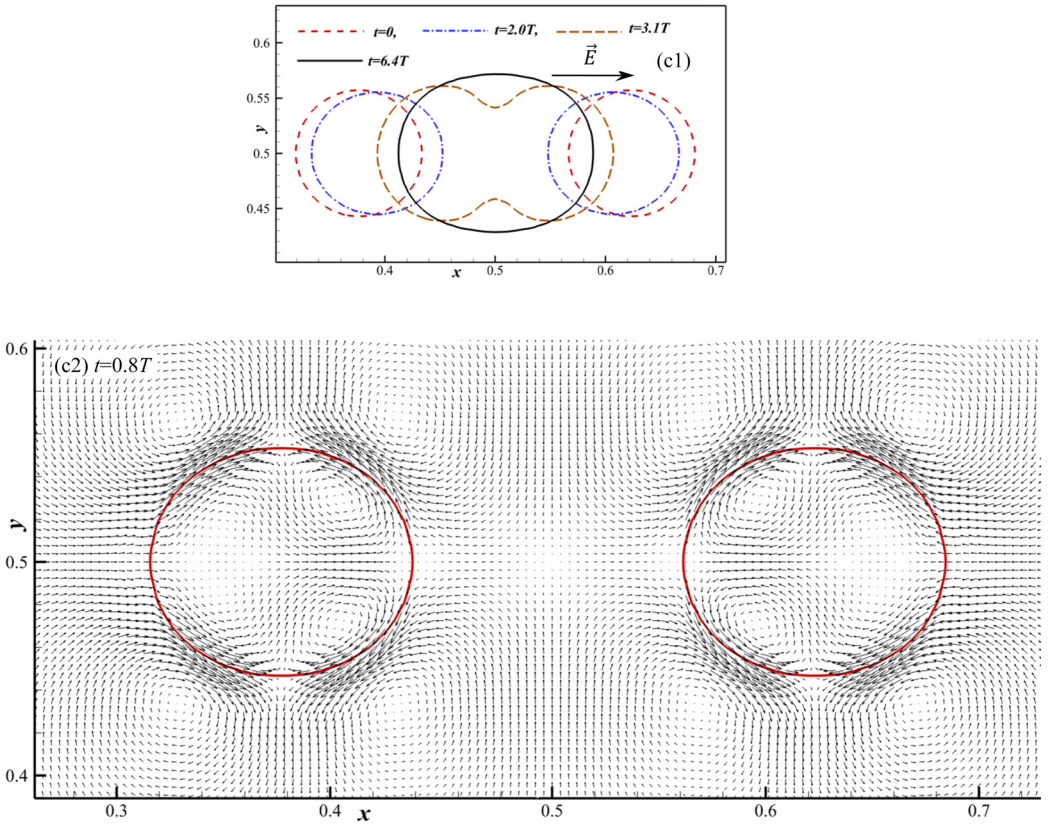

FIG. 5. *(Continued.)*

side [Fig. 5(a2)] enforce the left drop to move leftward through their induced higher velocity and overcomes the rightward forcing that is thrust upon by the relatively weaker right-side vortex pair situated just outside the interface. Therefore, the combined vortex dynamics-induced thrust causes the left drop to move leftward [Fig. 5(a1)]. In a similar way, the right drop is driven towards right due to combined dynamics of the developed inner and outer vortex pairs. Thus, from the perspective of simulated velocity vector field [Fig. 5(a2)], the drop pair at $\varepsilon_{\text{in}}/\varepsilon_{\text{out}} = 1.0, \sigma_{\text{in}}/\sigma_{\text{out}} = 5.0, \text{Ca}_E = 0.46$ ($d = 4R$) drifts apart under the effect of EHD interactions, and such finding agrees well with the existing theoretical analysis [26] for $\sigma_{\text{in}}/\sigma_{\text{out}} > \varepsilon_{\text{in}}/\varepsilon_{\text{out}}$; however the actual or hidden mechanism now becomes much clearer. As far as observed horizontal stretching of two drops (Fig. 5) to the *prolate* configuration is concerned, readers may note dominantly important roles of the *asymmetrically* developed near-interfacial two *outer vortex pairs* located at major axis ends. Owing to their induced outward dynamics or thrust (directed towards left and right) the drops are clearly forced to elongate or stretch *unequally* [Fig. 5(a1)] in the horizontal direction, leading to formation of a *prolate* shape while moving apart. Importantly, while the near-interfacial *outer vortex pairs* seating at major axis ends decisively dictate the horizontal drop elongation, the developed *inner vortex pairs* [Fig. 5(a2)] try to bring back the drops to an energy optimizing compact configuration through their induced motion or forcing. To be explicit, at major-axis ends of a deformed drop, where the local curvature is increased (radius of curvature decreased), the *inflow*-type two *inner vortex pairs* remain visibly active, and by virtue of induced inward forcing two *inflow*-natured *inner vortex pairs* try to resist the drop deformation (horizontal elongation). Furthermore, at minor-axis ends, where curvature is decreased (radius of curvature increased), the *outflow*-type local vortex dynamics prevails, and by outward local velocity or thrust the vortex pairs try to vertically stretch a drop to bring it back to a

stable circular shape. Notably, *for increasing* $\varepsilon_{in}/\varepsilon_{out}$ in the stretch A the above elaborated *repulsive strength* of the bulk flow (*via* developed *outer vortex pairs*) gradually decreases [see Eq. (11)] which results to reduced drop velocity u, as revealed by Fig. 4(c); in contrary, it clearly helps to enhance the *attractive electric force* [see Eqs. (12)–(14)].

Now we examine the EHD interactions in the stretch B ($2.4 < \varepsilon_{in}/\varepsilon_{out} < \sigma_{in}/\sigma_{out} = 5.0$). Note that, for progressively increased $\varepsilon_{in}/\varepsilon_{out}$ up to 5.0 [Fig. 4(c)] the deformed *prolate* drops move closer ($u < 0$) and coalesce due to increasing relative *dominance of electric interaction*. More precisely, a larger $\varepsilon_{in}/\varepsilon_{out}$ along stretch B [Fig. 4(c)] enhances the *attractive electric force* F_r [Eq. (12)], while *weakening the diverging* bulk fluid velocity. Accordingly, for $2.4 < \varepsilon_{in}/\varepsilon_{out} < \sigma_{in}/\sigma_{out} = 5.0$ the dominating electric interaction over the electrically driven hydrodynamic interaction leads drop pair to fast converge following increased [Fig. 4(c)] negative velocity ($-u$). Fig. 5(b1) illustrates the simulated nature of *electrocoalescence* for a drop pair at $\varepsilon_{in}/\varepsilon_{out} = 2.5$, that is, the transient drop-drop approach in stretch B [Fig. 4(c)]; showing that two drops at $\varepsilon_{in}/\varepsilon_{out} = 2.5$ deform *prolately* and then translate closer together and finally merge [Fig. 5(b1); $3.6 \leqslant t/T \leqslant 8.6$] into one *prolate* drop. Fig. 5(b2) shows the detailed interactive velocity field, at $t = 2.6T$, inducing the coalescence. Notably, inside the left drop, the vortex pair that developed in the left half appear stronger than the pair in right half, and resultant axial thrust of these two counterrotating pairs of *inner vortices* helps to drive the left drop rightward (along the direction of major axis). In addition, as revealed by relative length of outer velocity vectors [Fig. 5(b2)], on the left drop a decisively stronger rightward hydrodynamic thrust is clearly imposed by the induced motion of the dominating near-interfacial two *outer vortex pairs* (of bulk flow) that evolve symmetrically with respect to the major axis. Clearly the rightward forcing generated by the vortex pair situated at right end (owing to close proximity) overcomes the induced leftward axial thrust that is imposed by *vortex pair* formed at left end (of the left drop). Therefore, the combined (inner plus outer) vortex pairs driven resulting thrust enforces the left drop to move towards right. Similarly, the generated vortex pairs-induced forcing, as evident from Fig. 5(b2), effectively drives the right drop leftward. Owing to such electrohydrodynamic imbalance, and by virtue of enhanced *attractive electric force* [as F_r increased with $\varepsilon_{in}/\varepsilon_{out}$; Eqs. (12)–(14)], two deformed drops simultaneously move closer and eventually coalesce [Fig. 5(b1)] upon their contact. Moreover, the *prolate*-type drop deformation is primarily guided by oppositely directed dynamics [Fig. 5(b2)] of the *outflow*-natured near-interfacial two *outer vortex pairs* [e.g., Fig. 3(c)] that formed at major axis ends. Hereby, the resulting outer flows remained clearly and consistently directed from *equator to pole*, as postulated by Baygents *et al.* [26]. Remarkably, the consistent active roles of *inflow*- and *outflow*-natured vortex pairs in dictating unequal compression or elongation and *axis switching* for noncircular jet sections [52–55], and regulating solute entrainment in microdrops [56] are extensively elaborated in recent past. Solutions from the nonlinear set of governing equations and presented vortex dynamics based analysis thus provides an improved understanding of EHD responses that dictate coalescence and departure of the leaky dielectric drops. Physically, an *inflow-natured* vortex pair [52–55] of equal and opposite *strength* $\pm\boldsymbol{\Gamma}$ and *spaced* $2\boldsymbol{a}$ *apart* will exert an *inward force* proportional to $\boldsymbol{\Gamma/4\pi a}$, whereas an *outflow*-type [Fig. 3(c)] pair would exert the *outward force* $\sim\boldsymbol{\Gamma/4\pi a}$ to a drop.

In the stretch C [$5.0 < \varepsilon_{in}/\varepsilon_{out} < 9.57$; Fig. 4(c)] as $f_d > 0$ and $\sigma_{in}/\sigma_{out} < \varepsilon_{in}/\varepsilon_{out}$ the drops continue to display *prolate* deformation [26], but importantly the near-field EHD flow is changed to *pole-to-equator* [PR^-; Fig. 4(c)] owing to the 90° switched orientation of the dominant *outflow*-type outer vortex pairs. Accordingly, in C, the hydrodynamic force by bulk fluid and the electric force together influence the drop pair move closer and coalesce. For clarity, Figs. 5(c1) and 5(c2) show the drop pair's *prolate* coalescence and near-field flow behavior at $t = 0.8T$ and $\varepsilon_{in}/\varepsilon_{out} = 7.0$. Noteworthy, in Fig. 5(c2), is the vertically opposite directed *outflow*-natured dynamics of the developed two near-interfacial (weaker) outer vortex pairs; whereas in Fig. 5(b2) the motion of similar vortex pairs was horizontally directed. What we observed is that the stretch C display a transitional behavior and Fig. 5(c2) shows the transitional signature (at $Ca_E = 0.46$). Accordingly, as droplet deformation process starts to change from *prolate* to *oblate* shape, the favorable *outflow*-type two outer vortex pairs switch their orientation. Such issues are clarified again in Appendix C.

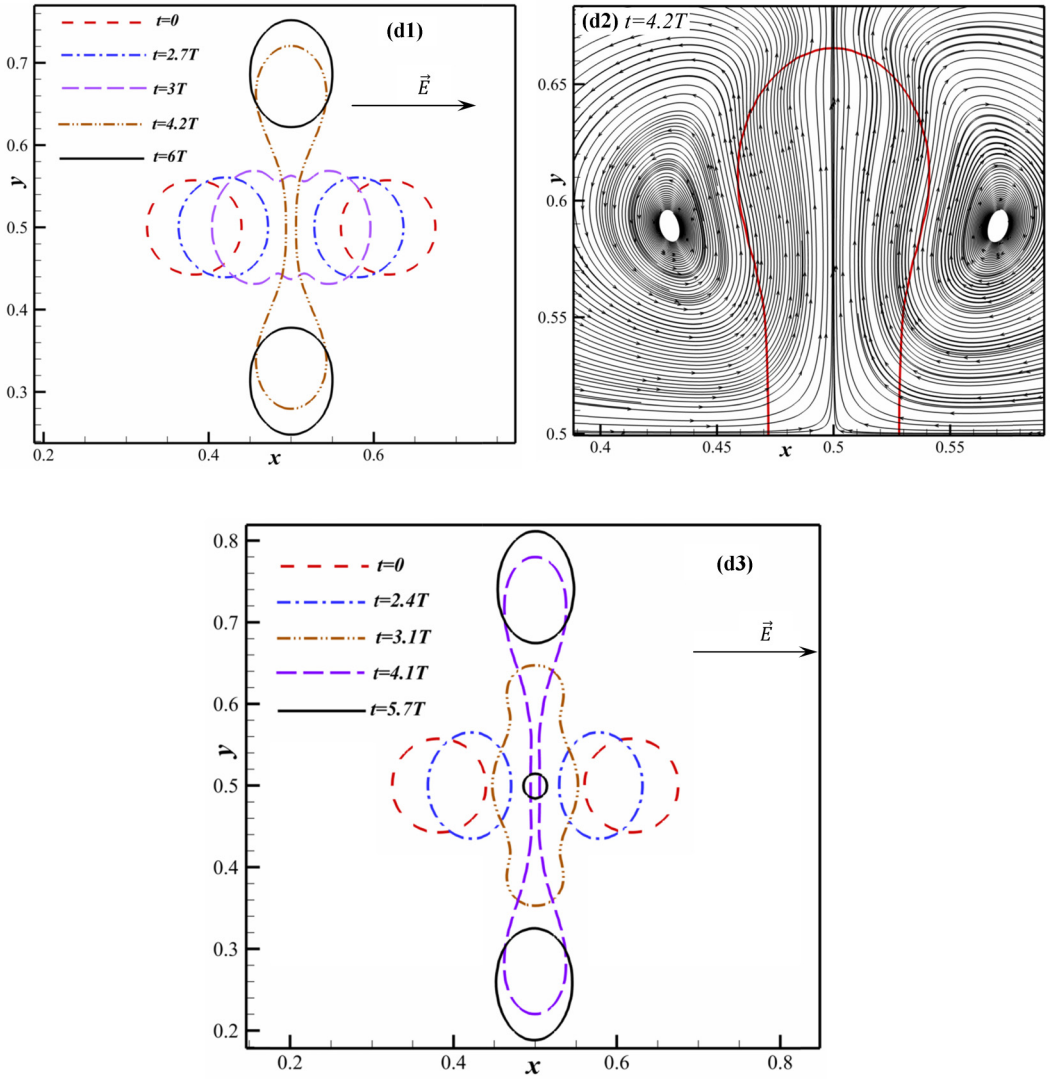

FIG. 6. The detected *oblate* deformation of a drop pair, transient *coalescence*, and the *postcoalescence* break up to different modes for increased $\varepsilon_{in}/\varepsilon_{out}$ over the stretch D $[(\varepsilon_{in}/\varepsilon_{out})_{crit3} = 9.57 < \varepsilon_{in}/\varepsilon_{out} \leqslant 20.0]$, at fixed $\sigma_{in}/\sigma_{out} = 5.0$, $Ca_E = 0.46$, $\alpha = 0^\circ$. (d1) The coalescence and subsequent two-component break up at $\varepsilon_{in}/\varepsilon_{out} = 11$, $Re = 1.71$; (d2) the streamlines at $t = 4.2T$ reveal the development of the *outflow*-natured vertically upward moving outer vortex pair around the upper half of the drop that drives it to elongate in a direction perpendicular to the electric field and facilitates breakup. Similarly, another *outflow*-natured downward moving near-interfacial outer vortex pair dominates around the bottom half of the drop. (d3) The detected *oblate* coalescence and three component breakup at $\varepsilon_{in}/\varepsilon_{out} = 15$, $Re = 2.85$. (d4) The transient coalescence and five component postcoalescing breakup at $\varepsilon_{in}/\varepsilon_{out} = 20$, $Re = 4.27$; and (d5) surrounding streamline pattern at $t = 3.48T$ reveal the active dominance or role of the developed vertically upward moving *outflow*-natured near-interface outer vortex pair that enforces the droplet to elongate in a direction orthogonal to the electric field due to the paired vortex-induced thrust. (d6) The corresponding velocity field at $t = 0.6T$ that facilitates drop pair to move closer and elongate in the vertical direction.

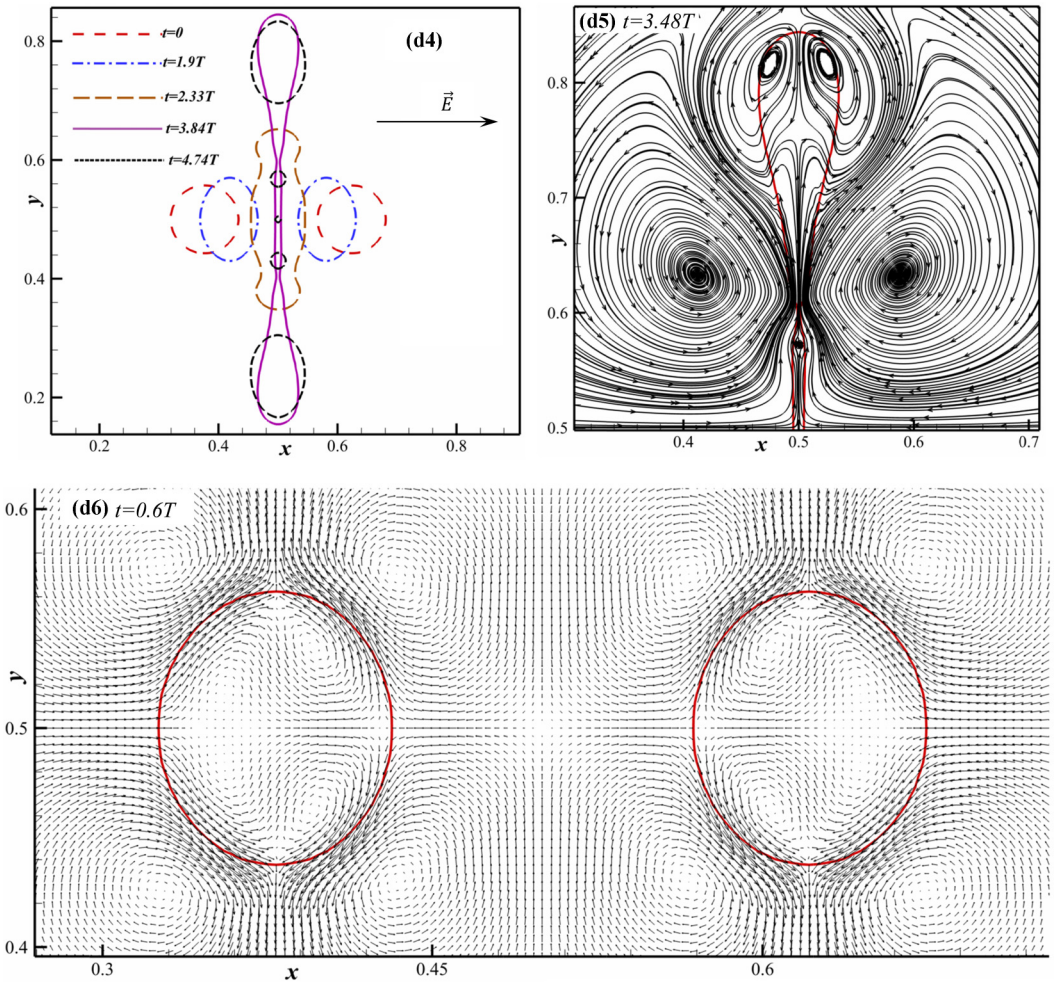

FIG. 6. *(Continued.)*

2. Relative motion, oblate coalescence of a drop pair, and breakup in stretch D

The new observation made here is that, for increased $\varepsilon_{in}/\varepsilon_{out} > (\varepsilon_{in}/\varepsilon_{out})_{crit3} = 9.57$ in the stretch D [Fig. 4(c)] the drop pair (at $Ca_E = 0.46$) first deform *oblately* and coalesce; and interestingly, upon coalescence the droplet disintegrates again in a direction perpendicular to the applied electric field. The detected such flow phenomena for different $\varepsilon_{in}/\varepsilon_{out}$ are extensively elaborated in Fig. 6. Our repeated and careful examination reveal, for gradually increased $\varepsilon_{in}/\varepsilon_{out} > (\varepsilon_{in}/\varepsilon_{out})_{crit3}$, the coalesced *oblate* drop breaks orthogonally to two satellite/component drops [Fig. 6(d1)] at $\varepsilon_{in}/\varepsilon_{out} = 11$, three satellite drops at $\varepsilon_{in}/\varepsilon_{out} = 15$ [Fig. 6(d3)], and five satellite drops at $\varepsilon_{in}/\varepsilon_{out} = 20$ [Fig. 6(d4)]. Apparently, the increased strength of electrohydrodynamic bulk flow and resulting augmented interfacial thrust as imposed by the *outflow*-natured vertically opposite moving two outer vortex pairs at $Ca_E = 0.46$ enforce the postcoalescence vertical drop elongation (Fig. 6) and eventual breakup. Such issues are elaborated below. Notably, Mhatre *et al.* [25] experimentally reported (Fig. 4 [25]) the postcoalescence breakup of a pair of castor oil drops (suspended in silicon oil) along the direction of applied electric field. According to Mhatre *et al.* [25] the increased Ca_E can influence such a breakup. In addition, in the experiment [25] $\sigma_{in}/\sigma_{out} = 50$ and $\varepsilon_{in}/\varepsilon_{out} = 1.77$ are used; that is, $\sigma_{in}/\sigma_{out} - \varepsilon_{in}/\varepsilon_{out} > 0$. This results to the horizontally opposite moving [e.g., Figs. 5(b2) and 3(b2)]

outer vortex pairs driven increased axial drop stretching at high $|\sigma_{in}/\sigma_{out} - \varepsilon_{in}/\varepsilon_{out}|$; possibly causing the postcoalescence horizontal drop breakup [25]. However, as shown in Fig. 6(d6), in stretch D [see Fig. 4(c)], with $\sigma_{in}/\sigma_{out} - \varepsilon_{in}/\varepsilon_{out} < 0$ and increasing difference of $|\sigma_{in}/\sigma_{out} - \varepsilon_{in}/\varepsilon_{out}|$, the bulk flow generates *outflow* paired vortex driven augmented vertically opposite EHD forcing at $\mathrm{Ca}_E = 0.46$, which leads to systematic elongation and multicomponent breakup [see Figs. 6(d1) and 6(d3)] of a coalesced drop in a direction perpendicular to the applied electric field. The unambiguous evidences are provided in this regard in Figs. 6(d2) and 6(d5), wherein the depicted streamlines around the upper half of coalesced drops explicitly reveal how exactly the upward moving near-interfacial *outflow*-natured outer vortex pairs decisively dictate vertical stretching and eventual postcoalescence drop breakup at $\varepsilon_{in}/\varepsilon_{out} = 11$, and $\varepsilon_{in}/\varepsilon_{out} = 20$, respectively (at a higher $\mathrm{Ca}_E = 0.46$).

Concerning the physical mechanism leading to encountered shape transformation, Fig. 6(d4) shows starting with $t > 0$ the leaky drop pair at $\varepsilon_{in}/\varepsilon_{out} = 20$ expand vertically (e.g., $t = 1.9T$) to an *oblate* shape and start moving closer ($u < 0$) at higher velocity [see Fig. 4(c)]. Subsequently, the coalesced drop elongates to a dumbbell shape at $t = 2.33T$ having fat belly and round edges. At $t = 3.84T$ two neck formations are clearly visible as the combined drop continues to vertically elongate; before eventually breaking to five satellite drops at $t = 4.74T$. Figure 6(d6) captures the simulated velocity field at $t = 0.6T$, showing the explicit nature of developed vortex driven near-field forcing or kinetics plus oblate deformation of two drops. Importantly, within the left drop we observe *asymmetric* (with respect to vertical centerline) presence of two vortex pairs; with left pair getting fast dissipated. The horizontal component of their induced internal velocity or thrust is clearly directed towards right. Second, at the left side of left drop, as Fig. 6(d6) reveals, the vortex-induced near-interface outer velocity or thrust remained rightward directed, while opposite natured velocity field at the central film region remains weaker. Therefore, owing to above mentioned two (inner and outer) -induced horizontal velocity components the left drop translates towards right. Similarly, for the right drop, clearly the horizontal component of the noted vortex pairs driven combined thrust (from inside plus outside) enforces it to move leftward [Fig. 6(d6)]. The physical process thereby guides two drops to gradually move closer and coalesce, *via* increased electric attraction F_r [Eq. (12)]. Third, as far as the vertical stretching to the *oblate* drop configuration is concerned, note in Fig. 6(d6) *the dominant roles of counterrotating two outflow paired outer vortices* (of bulk flow) seating at the top and at the bottom (of each drop). Note that, the vortex dynamics around a drop, as presented in Fig. 6(d6), corresponds to 90° rotated view of Fig. 3(c). The upward or downward directed motion and imposed thrust by the dominating two *outer vortex pairs* hereby decisively enforce continued physical stretching of the coalesced drop (Fig. 6) in a direction perpendicular to applied electric field. On the other hand, Fig. 6(d5) provides explicit flow details that clearly reveal the decisive role of the developed near-interfacial *outflow*-natured vertically upward moving outer vortex pair (that evolves around the neck) in dictating the observed drop breakup [Fig. 6(d4)]. The presented EHD flow simulations accordingly help to better comprehend the precise physics. Important to note that a nonbreaking or stable *oblate*-shaped drop-drop coalescence is indeed achievable by appropriately reducing the electric capillary number Ca_E; and Appendix C presents such computed details at $\mathrm{Ca}_E = 0.33$.

D. Physical insight into drop-drop electrocoalescence

The physically distinct stages of coalescence can be divided into (i) the approach of drop pair towards each other, (ii) the formation plus drainage of the film between approaching interfaces, and (iii) the rupture of the film [57]. The findings by Lin *et al.* [58] show natures of the near-field hydrodynamics and resulting various shapes of the leading drop face during film drainage for varied viscosity ratio (μ_{in}/μ_{out}). At high viscosity ratio ($\mu_{in}/\mu_{out} = 100$) a *protrusion* is formed at leading faces of the drop pair due to induced electric force; facilitating film drainage or rupture. In contrary, at low $\mu_{in}/\mu_{out} = 0.01 < 1.0$, the film drainage is obstructed due to high viscosity in the film, and the radical component of viscous stress that act on the interface generate the well-known *dimpled shape*. The phenomenon is also noted in the absence of electric filed [59,60]. Recently, Mhatre *et al.* [25] reported the formation of the dimpled shape during film drainage at $\mu_{in}/\mu_{out} = 2.28$, due

to increased tangential electric stress in a leaky dielectric system. Importantly, in our simulations as shown in Figs. 7(c1) and 7(c2), at a fixed $\mu_{in}/\mu_{out} = 1.0$ we detected the said two types of interfacial deformations during film drainage, by suitably tuning the conductivity ratio (σ_{in}/σ_{out}). At $\sigma_{in}/\sigma_{out} = 10.0$ [Fig. 7(c1)] the dimple shape formation is detected, and for $\sigma_{in}/\sigma_{out} = 5.0$ a protrusion developed [Fig. 7(c2)].

Now we focus on exploring near-contact or near-coalescence flow physics (at $\alpha = 0^\circ$). As observed by Bird *et al.* [23] upon initiation of coalescence of a drop pair, a low-pressure area forms within the neck region due to relatively smaller local curvature (positive), whereas higher pressure persists at respective drop center. This pressure difference drives inner fluid into neck region, and facilitates the coalescence [23]. In Fig. 7(a1)–7(b1), we capture the near-field pressure variation including both inside and outside of coalescing drops plus pressure distribution along the horizontal line ($y = 0.5$) of symmetry, when two drops are about to touch each other. The field properties used in simulation are $\varepsilon_{in}/\varepsilon_{out} = 2.5$, $\sigma_{in}/\sigma_{out} = 10$, $\mathrm{Ca}_E = 0.46$. The presented pressure contours in Fig. 7(a1) reveal, starting from contact line the pressure inside the drops gradually increases and reaches local maximum at two far ends. The pressure variation along the horizontal line of symmetry of the coalescing droplet as presented in Fig. 7(b1) displays the detailed physics. Clearly, the developed pressure gradient that is directed toward the neck hereby systematically drives inner fluid into the film region [Fig. 7(c1)] and stimulates the drop pair to coalesce. In addition, it's important to note in Fig. 7(a1) the existence of two distinct *outer high-pressure areas* that symmetrically formed across the neck, marked by outward directed arrows for clarity. Accordingly, the resulting vertically opposite local flow acceleration [23] helps the contact-line liquid bridge to expand outward and drain out the cavity fluid. For clarity, Fig. 7(c1) presents the EHD flow behavior surrounding the neck and the adjoin interface area at $\varepsilon_{in}/\varepsilon_{out} = 2.5$, $\sigma_{in}/\sigma_{out} = 10$, $\mathrm{Ca}_E = 0.46$. Herein, a distinct dent is noted in Fig. 7(c1), and in that a stronger tangential electric stress persists along the leading interface [25]. Noteworthy, in Fig. 7(c1), are the horizontally converging internal flow (that facilitates motion of respective drop centroids) towards the neck and the vertically outward continuous-phase film draining in the cavity region (e.g., Fig. 17 in Ref. [25]), in manners consistent to the experimental prediction of Mhatre *et al.* [25], under the influence of said pressure gradients that apparently expedite drop pair's coalescence. Note also in Fig. 7(c1), the roles of locally dominating two *outflow*-natured vortex pairs that actively regulate film drainage and interface expansion during the process of electrocoalescence, as the combined drop seeks to take a compact energy-optimized shape.

Remarkably, Fig. 1 of Sozou [51] shows the tangential electric stress on the leading drop face fast decreases, as conductivity ratio (σ_{in}/σ_{out}) is decreased. This reduction of tangential electric stress affects the shape of the contact line and the physical coalescence. To unravel the phenomenon, in Figs. 7(a2)–7(c2) we present the simulated pressure contour, streamline pattern, and the leading edge interface deformation characteristic as the coalescing drop pair is about to touch each other at a lower $\sigma_{in}/\sigma_{out} = 5.0$; while $\varepsilon_{in}/\varepsilon_{out} = 2.5$, $\mathrm{Ca}_E = 0.46$ remained unchanged. Notably, in this case, a stronger horizontal pressure gradient directed towards leading drop interface [Fig. 7(a2)] plus sharper transverse pressure (outer) variation across the neck region are generated at $\sigma_{in}/\sigma_{out} = 5.0$, compared to the case with $\sigma_{in}/\sigma_{out} = 10$ [Figs. 7(a1)–7(c1))]; prompting the formation of two characteristic Taylor cones and rupture of the film [Fig. 7(c2)] during coalescence. A protrusion is clearly formed at $\sigma_{in}/\sigma_{out} = 5.0$ on leading poles [Fig. 7(c2)], which is caused due to reduced tangential electric stress and increased horizontal pressure gradient [Figs. 7(a2)–7(b2)]. In addition, the issue of formation of Taylor cone for a single leaky drop (prior to breakup) is elaborated in Appendix D.

E. Effect of incidence angle α

The dispersion of drops often varies by wide ranges with respect to the direction of the applied electric field. Therefore, a better understanding of the α-dependent response of a drop pair is essential. As Eq. (12) shows, the radial electric force between two suspended leaky dielectric drops can have attractive ($\boldsymbol{F_r} > 0$) nature only when $3(\cos\alpha)^2 - 1 > 0$, i.e., for $\alpha < 54.7^\circ$ or $\alpha > 125.3^\circ$. Moreover, $\boldsymbol{F_t}$ and $\boldsymbol{F_r}$ [Eqs. (12) and (13)] induce a torque that causes two adjacent drops to exhibit

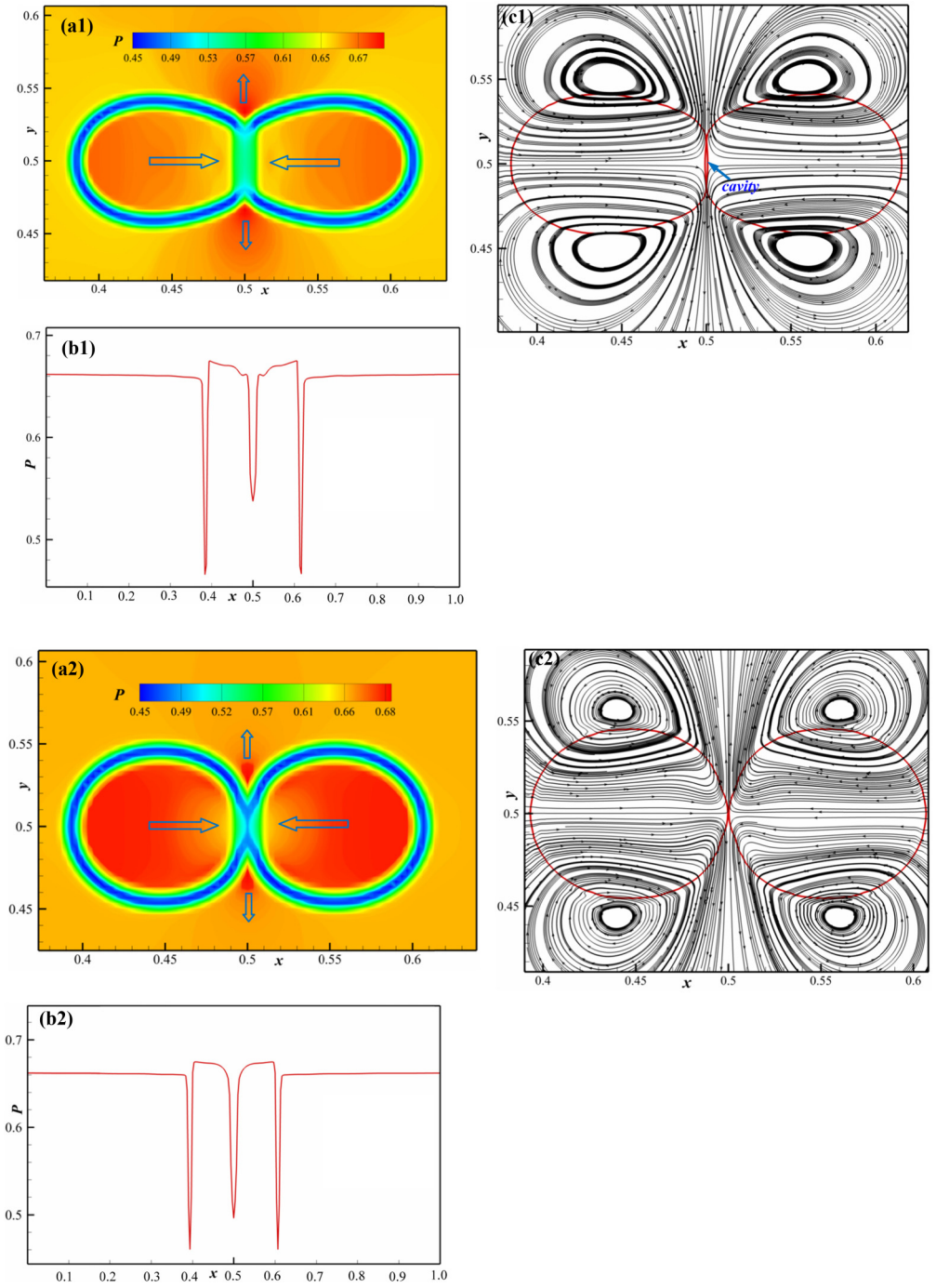

FIG. 7. (a1) The simulated pressure (p) contours; (b1) pressure variation along the horizontal line of symmetry $y = 0.5$; (c1) streamline pattern, and near-contact *dimple-shaped* interface deformation (red solid curve is the interface), as two drops begin to coalesce at $\sigma_{in}/\sigma_{out} = 10.0$, $\varepsilon_{in}/\varepsilon_{out} = 2.5$, $\mathrm{Ca}_E = 0.46$. (a2) The simulated pressure (p) contours; (b2) extracted pressure variation along the line $y = 0.5$; (c2) streamline patterns and near-contact *Taylor cone* formation at the interface (red solid curve is the interface), as two drops just begin to coalesce at a reduced $\sigma_{in}/\sigma_{out} = 5.0$; $\varepsilon_{in}/\varepsilon_{out} = 2.5$, $\mathrm{Ca}_E = 0.46$.

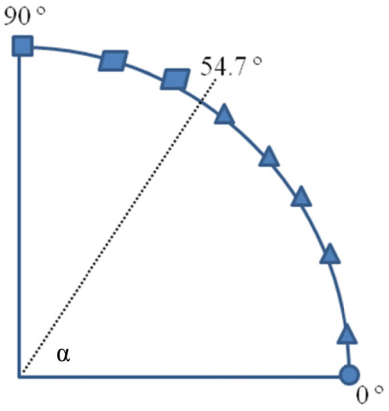

FIG. 8. Mutual responses of a drop pair aligned at different angles α to the applied electric field: attraction (●); attraction and rotation (▲); repulsion (■); repulsion and rotation (▰).

rotating motion. The available experimental results [24,25] suggest such a coupled dynamics for nonaligned drop pairs. However, the governing EHD interaction and possible *prolate* or *oblate* drop deformation remained unexplored, and there virtually exists no computational contribution. As a first step, systematic 2D simulations are done to reveal the α-dependent response (for $\mathrm{Re} \leqslant 1.48$) of two identical leaky dielectric drops in an immiscible leaky dielectric medium. Considering symmetry of drop pairs appearing at α and $180°-\alpha$ in a horizontally aligned electric field, the variation of α through $0° \leqslant \alpha \leqslant 90°$ is examined first for fixed center-to-center distance $d = 5R$ of two drops, and at $\varepsilon_{\mathrm{in}}/\varepsilon_{\mathrm{out}} = 0.9$, $\sigma_{\mathrm{in}}/\sigma_{\mathrm{out}} = 0.5$, $\mathrm{Ca}_E = 0.76$. The simulated characteristic response of a drop pair for $0° \leqslant \alpha \leqslant 90°$ are presented in Fig. 8, which clearly agree with existing experimental predictions for anchored drops [24] and for water or castor-oil drops suspended in silicone oil [25]. Notably, two classes of behavior, attraction and repulsion, depending on the initial angle α are observed (Fig. 8). For $0° < \alpha < 54.7°$, the attractive radial component $\boldsymbol{F_r}$ of electric force drives two drops closer during transient electrocoalescence. However, the tangential component $\boldsymbol{F_t}$ effectively manipulates the drop pair to rotate and eventually align with the direction of the applied electric field. Accordingly, during coalescence the deformed drop pair (Fig. 9) mutually converge while gradually lowering α to zero. On the other hand, for $54.7° < \alpha < 90°$ (Fig. 8), the drop pair is pushed apart (e.g., Fig. 10) under the influence of developed repulsive radial force $\boldsymbol{F_r}$; and $\boldsymbol{F_t}$ made them rotate while moving away. At $\alpha = 0°$ or $\alpha = 90°$ only the radial force component [Eqs. (12) and (13)] exists, and drops can have no rotational motion. Accordingly at $\alpha = 0°$ or $\alpha = 90°$ the EHD responses appear similar those presented in Sec. III C. Importantly, as evidenced below, for $0° < \alpha < 54.7°$ and suitably selected dielectric properties the coalescing drops reveal the systematic shape transformation from an eight style to final *oblate or prolate* state.

To better display the α-dependent mutual interactions for leaky dielectric drop pairs, the simulated EHD flow phenomena are extensively presented in Figs. 9–11. At $\alpha = 35°$, a sketch denoting the attractive electric force ($\boldsymbol{F_e}$), together with equivalent radial ($\boldsymbol{F_r}$) and tangential ($\boldsymbol{F_t}$) force components that exerted at drop centers is provided in Fig. 9(a). Under the influence of said forces ($\boldsymbol{F_r}$ plus $\boldsymbol{F_t}$), the detected rotating motion, *oblate* deformation, and coalescence of two drops at $\varepsilon_{\mathrm{in}}/\varepsilon_{\mathrm{out}} = 0.9$, $\sigma_{\mathrm{in}}/\sigma_{\mathrm{out}} = 0.5$, $\mathrm{Ca}_E = 0.76$, $\alpha = 35°$ are illustrated in Fig. 9(b). Importantly, the drops first deform to *oblate* shape through $0.0 < t \leqslant 0.5T$, prior to initiation of relative motion of their mass centers, and then the attractive radial component ($\boldsymbol{F_r}$) of electric force drives them closer by gradually reducing the center-to-center gap. However, under the effect of $\boldsymbol{F_t}$ [Eq. (13)] a torque is produced [see Fig. 9(c2)]; which acts to align the drop pair along the direction of the applied electric field by slowly reducing α to zero at coalescence. Thereby, the drop pair exhibits *rotating coalescence* as noted in Fig. 9(b). For clarity, detailed EHD interaction process in the form of

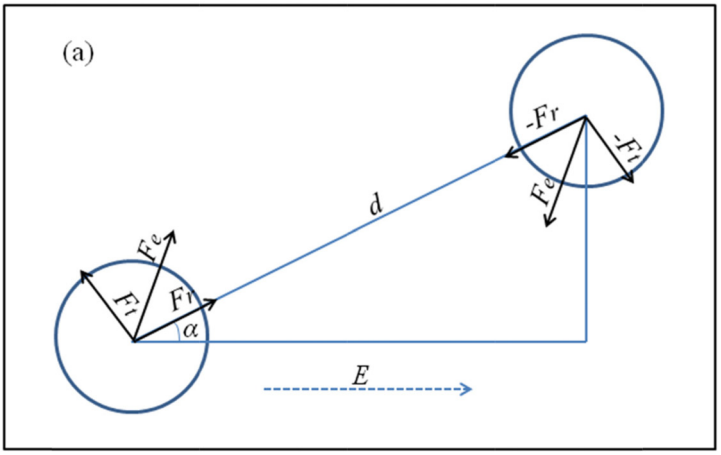

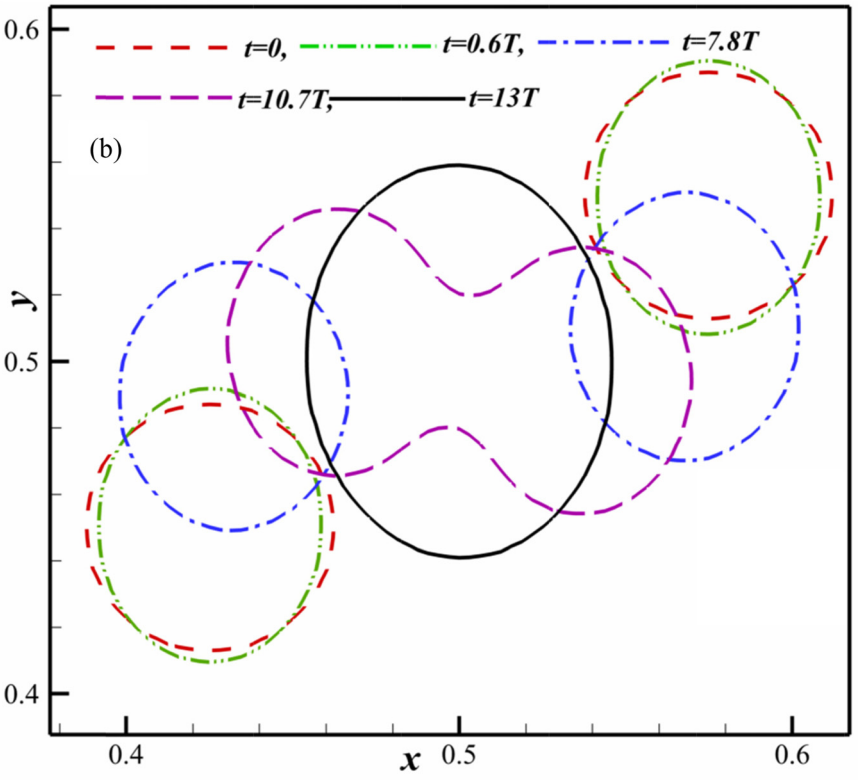

FIG. 9. (a) Sketch of the *attractive* electric force $\boldsymbol{F}_e$ acting on two drops placed at an angle $\alpha = 35^\circ$ with the direction of electric field; $\boldsymbol{F}_e$ is the total force, and $\boldsymbol{F}_r$, $\boldsymbol{F}_t$ correspond to radial and tangential force components shown to act at drop centers. (b) Simulated transient alignment and *coalescence* of a drop pair to an *oblate* shape. (c1) The induced vortical velocity field around the left drop at $t = 8.9T$ (red solid curve is the drop interface). (c2) The combined streamline plot at $t = 8.9T$ around two drops revealing the physical process of rotating *coalescence* at $\alpha = 35^\circ$. (d) The velocity vector plot at $t = 10.7T$ shows the role of the developed two *outflow*-natured vortex pairs in the interface expansion process upon merging. $\varepsilon_{\text{in}}/\varepsilon_{\text{out}} = 0.9$, $\sigma_{\text{in}}/\sigma_{\text{out}} = 0.5$ and $\text{Ca}_E = 0.76$, $\text{Re} = 1.39$, $d = 5R$.

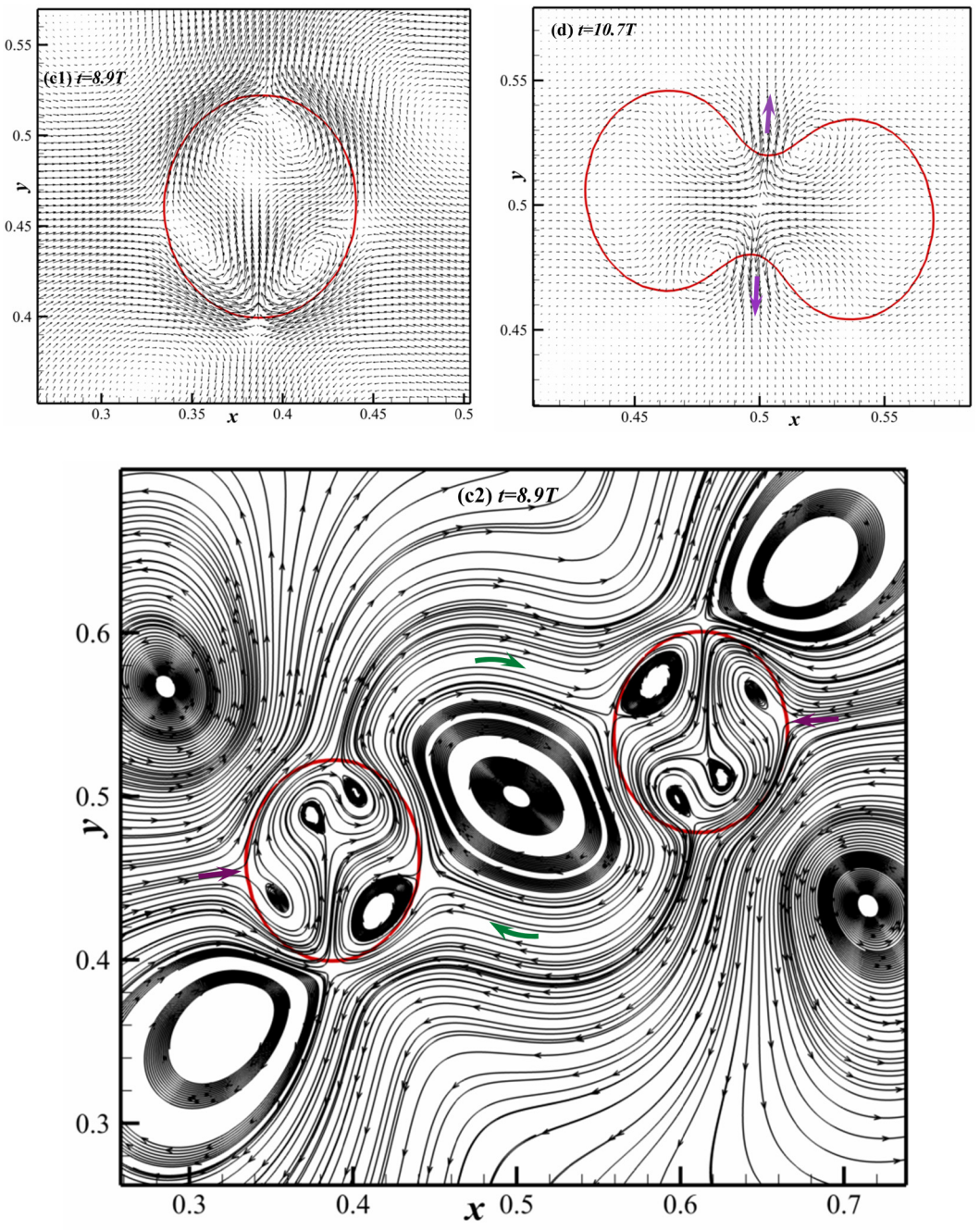

FIG. 9. *(Continued.)*

generated instantaneous velocity field in a drop (the left drop), and the combined streamline pattern surrounding the deformed or moving drop pair ($\alpha = 35^\circ$) at $t = 8.9T$ is presented in Figs. 9(c1) and 9(c2). As Fig. 9(c1) shows, under the influence of radial ($\boldsymbol{F_r} > 0$, attractive) and tangential ($\boldsymbol{F_t}$) forces [Eqs. (12) and (13)] the *asymmetric* velocity field (with respect to horizontal centerline) that develops in the left drop, *via* the dynamics of two pairs of *asymmetrically* evolving *inflow-natured inner*

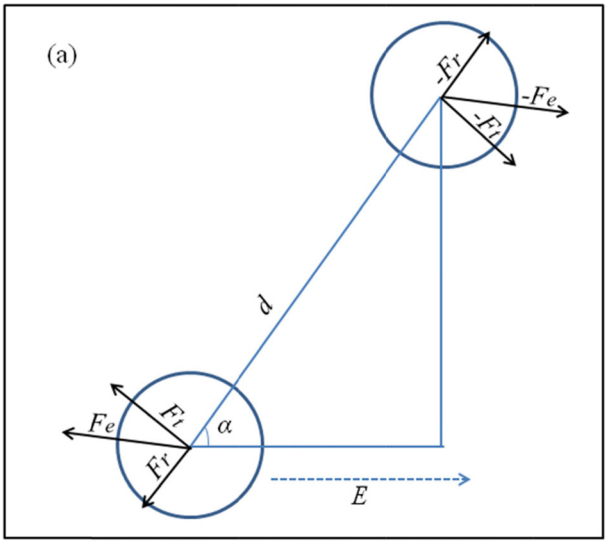

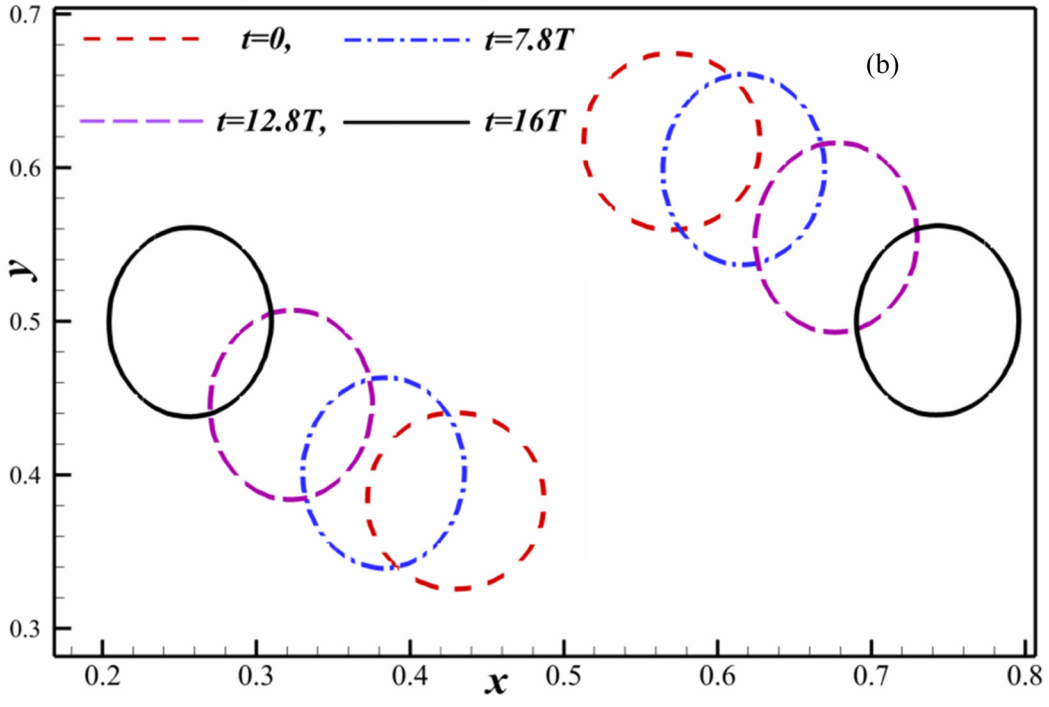

FIG. 10. (a) Sketch of a *repulsive* electric force acting on the drop pair at $\alpha = 60^\circ$; $\boldsymbol{F_e}$ is the total force, and $\boldsymbol{F_r}$, $\boldsymbol{F_t}$ correspond to radial and tangential components shown to act at drop centers. (b) Simulated temporal *divergence* process of deformed *oblate* drop pair. (c) The developed velocity field around the left drop at $t = 7.9T$ (red solid curve is the drop interface). (d) The combined streamlines at $t = 7.9T$, revealing the clockwise rotating divergence of the *oblate* drop pair at $\alpha = 60^\circ$. $\varepsilon_{\text{in}}/\varepsilon_{\text{out}} = 0.9$, $\sigma_{\text{in}}/\sigma_{\text{out}} = 0.5$, $\text{Ca}_E = 0.76$, $\text{Re} = 1.39$, $d = 5R$.

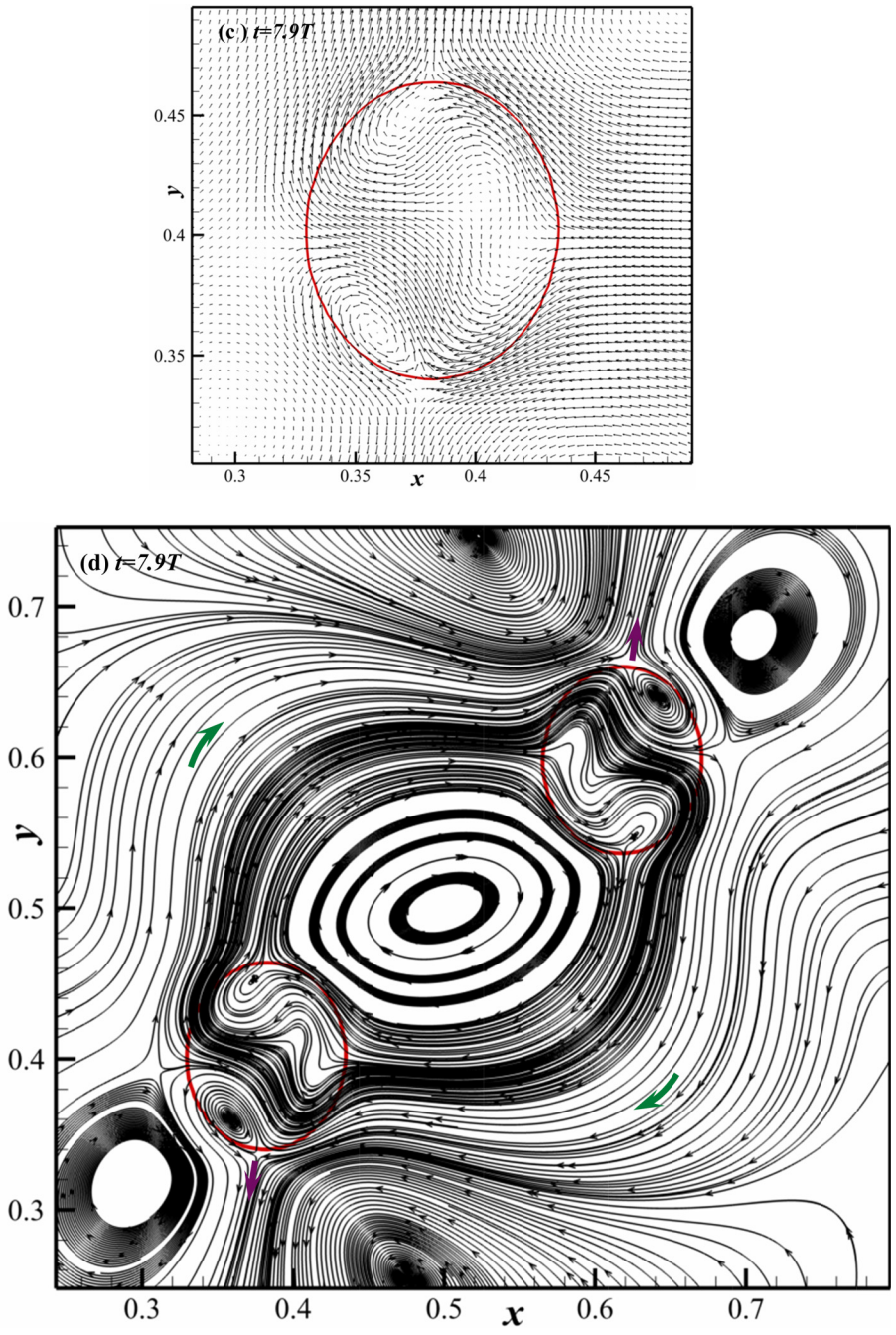

FIG. 10. *(Continued.)*

vortices, remains predominantly upward directed. On the other hand, the dominantly asymmetric and opposite moving near-interfacial *outflow*-type two outer vortex pairs (seated at top and bottom) decisively stretch the left drop vertically [Fig. 9(c1)] to produce an *oblate* shape. As Figs. 9(c1) and 9(c2)] show, the dominating *outflow*-natured outer vortex pairs-induced thrust is responsible for lifting the left drop upward in a rightward tilted manner under $\boldsymbol{F}_t$. Such upward motion occurs, as the

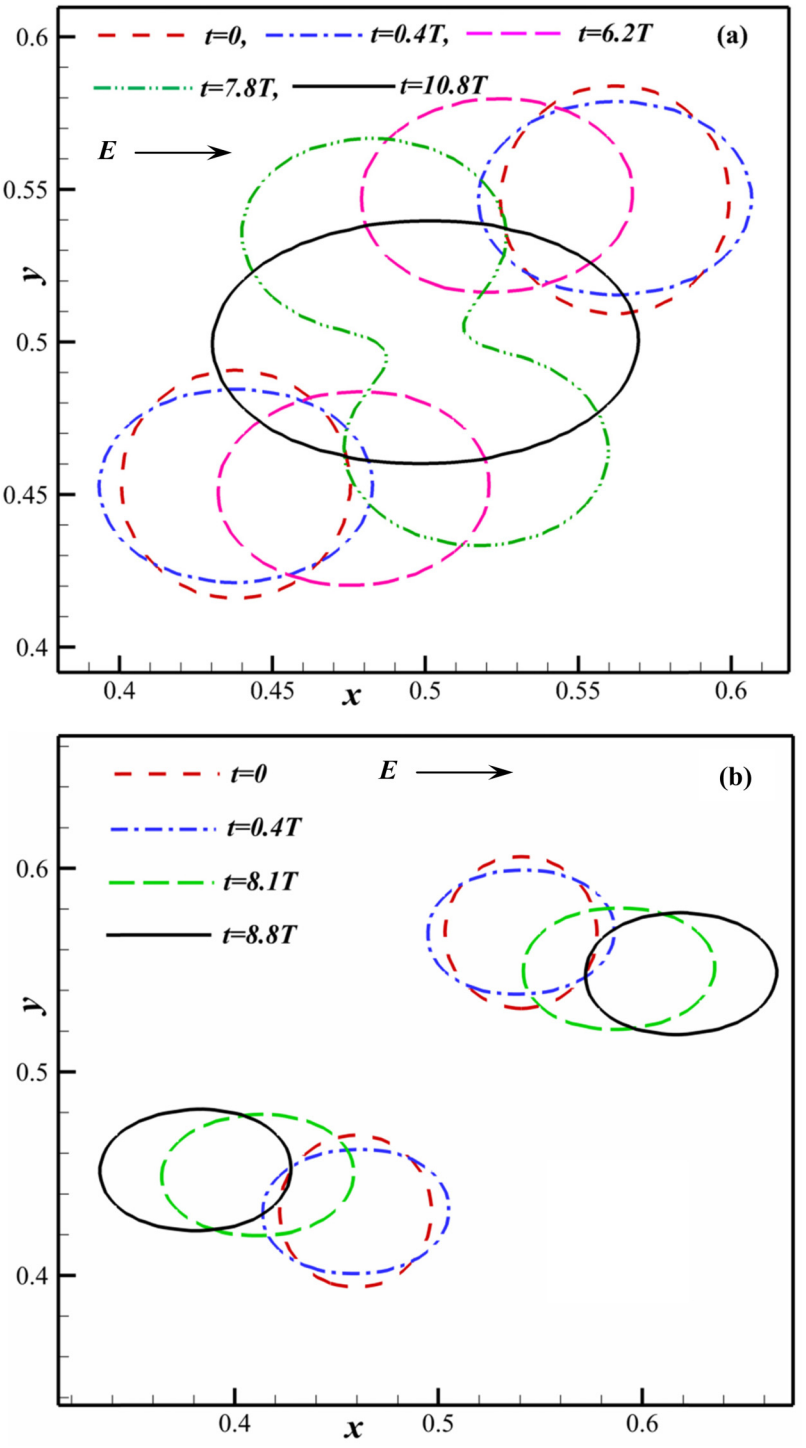

FIG. 11. (a) Simulated transient alignment and *coalescence* of the deformed *prolate* drop pair at $\alpha = 35^{\circ}$; (b) simulated *divergence* of the deformed *prolate* drop pair at $\alpha = 60^{\circ}$. $\varepsilon_{\text{in}}/\varepsilon_{\text{out}} = 0.9, \sigma_{\text{in}}/\sigma_{\text{out}} = 2.0, \text{Re} = 1.48$, $\text{Ca}_E = 1.0$. Note that, the physical domain size is much larger, however, for clarity we capture a small part of it.

outflow-natured outer vortex pair that formed at the upper edge of the drop interface appears relatively closely placed and stronger [Fig. 9(c1)] than the *outflow*-type outer vortex pair formed below the lower edge. Moreover, Fig. 9(c1) shows the resulting horizontal component of velocity (from left and right) surrounding the left drop remains rightward directed. Therefore, under $\boldsymbol{F_r}$ and $\boldsymbol{F_t}$ the left drop moves rightward [Fig. 9(b)] with time, while α is systematically decreased. Similarly, the other drop situated at right side [Fig. 9(c2)] faces an equal but opposite force that brings it closer to the left drop, while α is slowly reduced to zero. Accordingly, the left drop exhibits the upward motion whereas the right drop follows an equal downward motion and produce *clockwise rotating oblate coalescence* [Fig. 9(b)], under $\boldsymbol{F_r}$ and $\boldsymbol{F_t}$. Notably, for the chosen set of parameters the induced hydrodynamic force, as evident from Fig. 9(c2), becomes favorable and leads to the *oblate coalescence* of the leaky dielectric drops at $\alpha = 35^\circ$. Clearly, the manifestation of numerically generated flow behavior adds value to the available experimental predictions [24,25]; and the governing flow phenomena now becomes easier to realize. Moreover, Fig. 9(d) shows clear role of timely important two *outflow*-type vortex pairs in facilitating the outward interface expansion at the neck region, as the combined drop try to attend an energy optimizing shape.

Once α is increased (Fig. 8) beyond the critical angle 54.7° the $\boldsymbol{F_r}$ [<0; Eq. (12)] acts repulsively and drives the drop pair apart [Figs. 10(a) and 10(b)]. Owing to coupled tangential [Eq. (13)] force $\boldsymbol{F_t}$ (that tends to align the drop pair with the applied electric field) and radial force $\boldsymbol{F_r}$, both drops at this stage drifts apart while exhibiting rotation during transient motion. Figure 10(b) presents simulated such drop-drop departure with *oblate* deformation, at $\alpha = 60^\circ$ and $\varepsilon_{\text{in}}/\varepsilon_{\text{out}} = 0.9$, $\sigma_{\text{in}}/\sigma_{\text{out}} = 0.5$, $\text{Ca}_E = 0.76, d = 5R$. The vortical velocity field in a deformed drop (left drop) and the outer EHD flow pattern that induce the predicted motion plus *oblate* shape of the drop pair at $t = 7.9T$ are revealed in Figs. 10(c) and 10(d). Notably, the developed velocity field around the *left drop*, as shown in Fig. 10(c), clearly facilitates the leftward motion of its mass center under $\boldsymbol{F_r}$ and $\boldsymbol{F_t}$. Conversely, the drop situated on right side experiences a net force that is directed rightward. Furthermore, as Fig. 10(d) shows, the *oblate* drop pair in this case rotate clockwise owing to imposed tangential component ($\boldsymbol{F_t}$) of the electric force [Eq. (13)]; helping to reduce the angle of inclination (α) during mutual divergence. The deformed *oblate* drop pair [Fig. 10(b)] accordingly moves apart under $\boldsymbol{F_r}$ [<0; Eq. (12)] and $\boldsymbol{F_t}$ [Eq. (13)], following the elaborated EHD interaction at $\alpha = 60^\circ$.

Figure 11 shows the simulated electrocoalescence or departure of two nonaligned ($\alpha \neq 0^\circ$) leaky drops, as they deform *prolately* for suitably selected dielectric properties. The initial center-to-center distance (d) of the drops is taken as $d = 5R$. As Fig. 11(a) exhibits, the drop pair placed at $\alpha = 35^\circ$ and for chosen dielectric properties, $\varepsilon_{\text{in}}/\varepsilon_{\text{out}} = 0.9$, $\sigma_{\text{in}}/\sigma_{\text{out}} = 2.0$, $\text{Ca}_E = 1.0$, now experience *anticlockwise rotating prolate coalescence*, while their inclination is systematically reduces to zero. The attractive $\boldsymbol{F_r}$ [>0; Eq. (12)] in this case drives the drop pair closer, whereas $\boldsymbol{F_t}$ [Eq. (13)] produces a torque that acts to align the drops with the direction of the electric field. On the other hand, as α is increased to $\alpha = 60^\circ$, the $\boldsymbol{F}_r(<0)$ became repulsive, and the same drop pair [Fig. 11(b)] with identical properties, $\varepsilon_{\text{in}}/\varepsilon_{\text{out}} = 0.9$, $\sigma_{\text{in}}/\sigma_{\text{out}} = 2.0$, $\text{Ca}_E = 1.0$, *move apart prolately* during the EHD interaction. Since the electric interaction and the *inflow or outflow*-natured vortex pairs driven near-field hydrodynamic phenomena remained consistent to those presented in Figs. 9 and 10, the details are omitted here for the sake of brevity. However, Figs. 9–11 clearly display the electro*coalescence or departure* behaviors of nonaligned leaky drop pairs that depend solely on angular orientation α (Fig. 8); whereas the appropriately selected dielectric or field properties here distinctly influence the *oblate*- (Figs. 9 and 10) and the *prolate*- (Fig. 11) type structural deformations.

IV. CONCLUSIONS

In this study, the interparticle explicit forcing LBM model is implemented to numerically investigate the EHD response of the leaky dielectric drops in another immiscible leaky dielectric fluid under the applied electric field. Using full nonlinear equations and widely varied dielectric properties, the work uncovers precise electrohydrodynamic interactions that regulate observed *prolate and oblate* drop deformations, dispersion, coalescence, and postcoalescence breakup phenomena. The present

study reveals that, the *outflow*-natured two outer vortex pairs of the bulk flow that are created due to tangential electric stress effectively lead to *prolate* and *oblate* drop deformations, depending on conductivity (σ_{in}/σ_{out}) and permittivity ($\varepsilon_{in}/\varepsilon_{out}$) ratios of drop fluid to surrounding fluid. First, for an *isolated drop* we simulate the *prolate* to *oblate* shape transformation. At fixed $\varepsilon_{in}/\varepsilon_{out} = 10$, $Ca_E = 0.18$, when σ_{in}/σ_{out} is increased from 1.81 to 14.5, the *isolated leaky drop* transforms from an *oblate* shape (at $\sigma_{in}/\sigma_{out} = 1.81$) to a *prolate* shape (at $\sigma_{in}/\sigma_{out} = 14.5$). Our results show that, the persisting symmetrical dominance of two opposite moving *outflow*-type EHD *vortex pairs* at major axis ends of a *prolate* or *oblate* drop, and their 90° switching distinctly lead to *prolate*- and *oblate*-shaped drop deformations; while the resulting outer flow remained directed from *equator to pole* and *pole to equator*, respectively.

Second, the coupled interactions of suspended leaky dielectric drop pairs at $\alpha = 0°$ reveal interesting interdependence of relative drop velocity (u) and permittivity ratio ($\varepsilon_{in}/\varepsilon_{out}$) in $0.25 \leqslant \varepsilon_{in}/\varepsilon_{out} \leqslant 20.0$, when $\sigma_{in}/\sigma_{out} = 5.0$, $Ca_E = 0.46$ kept fixed; unfolding two physically distinct driving mechanisms. While the dipolar (attractive) electric force try to bring the drop pair closer, the imbalance created by the electrically driven hydrodynamic force (vortical outer flows) depending on the sign of $\sigma_{in}/\sigma_{out} - \varepsilon_{in}/\varepsilon_{out}$ made two drops move either closer or apart. At $\varepsilon_{in}/\varepsilon_{out} = 1.0$, $\sigma_{in}/\sigma_{out} = 5.0$, $Ca_E = 0.46$ [for $\varepsilon_{in}/\varepsilon_{out} < (\varepsilon_{in}/\varepsilon_{out})_{crit1} = 2.4$, as hydrodynamic force dominated over attractive electric force] the horizontally opposite directed two dominant *outflow*-natured *outer vortex pairs*, situated at left end of left drop and right end of right drop, decisively forced the *prolately* deformed drops move away ($u > 0$) from each other. With increased $\varepsilon_{in}/\varepsilon_{out}$ until a critical value $(\varepsilon_{in}/\varepsilon_{out})_{crit1} = 2.4$, the electrical shear stress-induced hydrodynamic vortex pairs (at fixed $\sigma_{in}/\sigma_{out} = 5$, $Ca_E = 0.46$) could generate a decisive repulsive force (that exceeded attractive electrical interaction) *via* their dominant *outflow*-type outward dynamics (induced thrust), and force the deformed (*prolate*) drop pair move apart. However, for $2.4 = (\varepsilon_{in}/\varepsilon_{out})_{crit1} < \varepsilon_{in}/\varepsilon_{out} < \sigma_{in}/\sigma_{out} = 5.0$ the dipolar (attractive) electric force dominated over relatively weakened hydrodynamic force, which made the drop pair (having initial separation distance $d = 4R$) move closer ($u < 0$) and coalesce to a *prolate* form. As far as near-coalescing flow physics is concerned, the present results exhibit that the development of local low pressure in neck region of two coalescing drops, compared to high pressure that persists at respective drop centers, creates the favorable pressure gradient to transport the inner fluid into the neck and facilitates the electrocoalescence. Importantly, for $\varepsilon_{in}/\varepsilon_{out} > \sigma_{in}/\sigma_{out}$ the direction or orientation of the dominating *outflow* paired outer vortex dynamics and the induced thrust switched by 90°; however, a coalesced drop could preserve the *prolate* shape for permittivity ratios ($\varepsilon_{in}/\varepsilon_{out}$) ranging over $\sigma_{in}/\sigma_{out} = 5.0 < \varepsilon_{in}/\varepsilon_{out} < (\varepsilon_{in}/\varepsilon_{out})_{crit3} = 9.57$.

Third, for $\varepsilon_{in}/\varepsilon_{out} > 9.57$ the drop pair not only deformed and coalesced to an *oblate* shape; importantly, at this higher $Ca_E = 0.46$, upon electrocoalescence the elongated *oblate* drop broke again into a number of satellite drops spreading in a direction perpendicular to the applied electric field. For gradually increased permittivity ratio ($\varepsilon_{in}/\varepsilon_{out} > 9.57$) the coalesced *oblate* drop broke (orthogonally) to two satellite drops at $\varepsilon_{in}/\varepsilon_{out} = 11$, three satellite drops at $\varepsilon_{in}/\varepsilon_{out} = 15$, and five satellite drops at $\varepsilon_{in}/\varepsilon_{out} = 20$. The increased strength of electrohydrodynamic bulk flow (at $Ca_E = 0.46$) and the resulting *outflow* paired vertically opposite vortex motion-induced augmented thrust seem to govern this *postcoalescence drop breakup*.

Four, the coalescence of the nonaligned ($\alpha \neq 0$) leaky drops depends significantly on the angle α between the directions of applied electric field and the line joining mass centers of two drops. For $\alpha < 54.7°$ or $\alpha > 125.3°$, the dipolar electric interaction-induced an attractive radial force along the line joining mass centers of two drops, while the tangential force components created a torque; which enforced the drop pair move closer and eventually align with the applied electric field upon coalescence. For $54.7° < \alpha < 125.3°$ the growth of repulsive radial component of dipolar electric force effectively pushed the drop pair apart. Our simulations at $\alpha = 35°$ and $\alpha = 60°$ exhibit, for $\varepsilon_{in}/\varepsilon_{out} = 0.9$, $\sigma_{in}/\sigma_{out} = 0.5$, $Ca_E = 1.0$ ($\sigma_{in}/\sigma_{out} - \varepsilon_{in}/\varepsilon_{out} < 0$) the coalescing or diverging drop pair deform *oblately*, whereas at $\varepsilon_{in}/\varepsilon_{out} = 0.9$, $\sigma_{in}/\sigma_{out} = 2.0$, $Ca_E = 1.0$ ($\sigma_{in}/\sigma_{out} - \varepsilon_{in}/\varepsilon_{out} > 0$) the drops took the *prolate* shape. Importantly, while remaining consistent to past predictions, the present simulations using the implemented nonlinear model provide significant new insights into

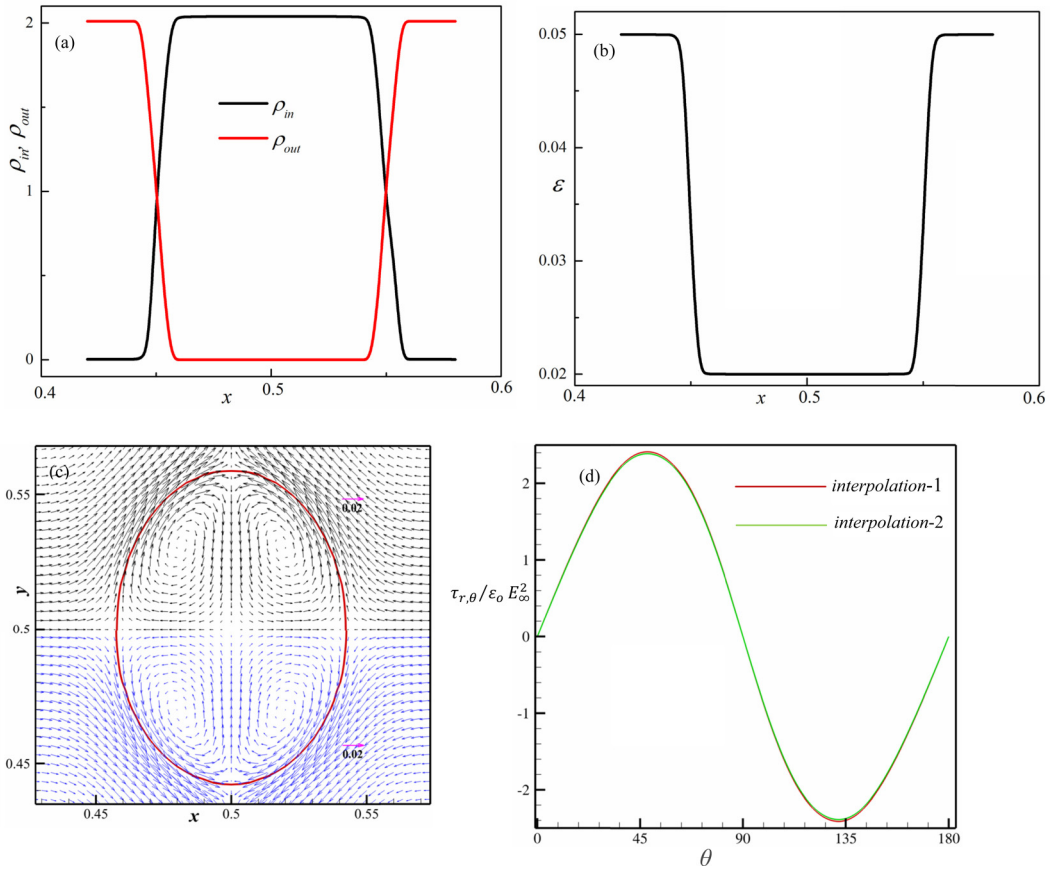

FIG. 12. Using interpolation 1 [Eq. (29)], the computed (a) density, and (b) permittivity (ε) profiles across the drop interface and along the horizontal line of symmetry $y = 0.5$. (c) Simulated drop deformation and velocity field obtained by adopting two different interpolation schemes: for the top half the interpolation 1 is used, and for the bottom half the interpolation 2 [Eq. (A1)] is used to calculate the electric properties; (d) computed tangential electric stress obtained by adopting interpolation 1 [Eq. (29)] and interpolation 2 [Eq. (A1)].

physical coalescence, departure, and breakup details of leaky EHD drops for widely varied dielectric properties and incidence angle.

ACKNOWLEDGMENT

The work is supported by NRF Grant No. 2017R1D1A1A09000952, Republic of Korea.

APPENDIX A: SMOOTHENING OF FLUIDIC PROPERTIES IN THE TRANSITION REGION

Based on Eq. (29), that is the interpolation 1, and using $\varepsilon_{\text{in}} = 0.02$ and $\varepsilon_{\text{out}} = 0.05$, Fig. 12(a) and 12(b) present the computed distributions of ρ_{in}, ρ_{out}, and ε along the horizontal drop centerline, spanning across fluid-fluid interfaces. Such variations of ρ_{in}, ρ_{out} [Fig. 12(a)] and ε [Fig. 12(b)] are used to generate smooth transition of properties across an interface, from one bulk value to another. However, a cosine function interpolation is used in the past [see Eq. (12) in Trau *et al.* [36]] to describe the transition of physical properties. In order to demonstrate the insensitivity of the computed results to the density profile [e.g., Eq. (29)] we change the interpolation scheme to a proposed new one

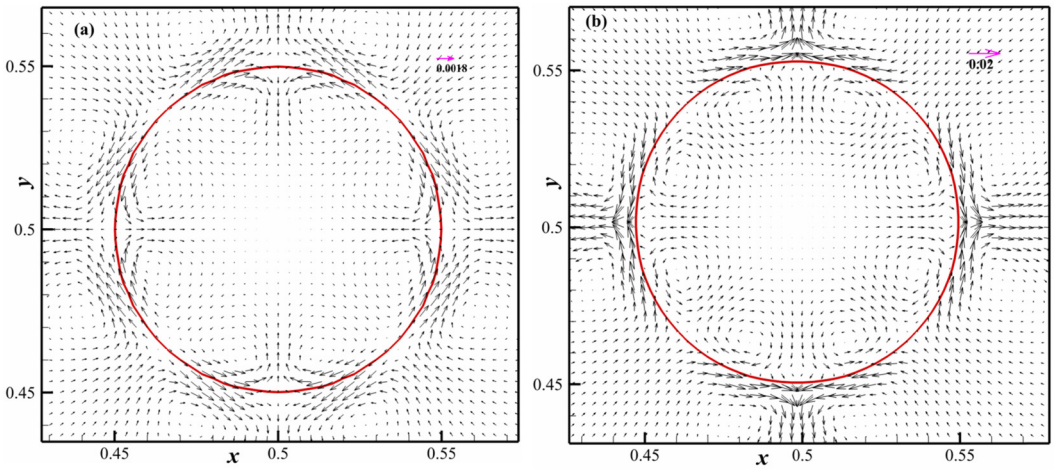

FIG. 13. Comparison of spurious currents [39] generated by (a) the present explicit forcing model, and (b) the Shan and Chen [33] model, for a static droplet.

[interpolation 2; Eq. (A1)], expressed as

$$\rho\varepsilon^2 = \rho_{\text{in}}\varepsilon_{\text{in}}^2 + \rho_{\text{out}}\varepsilon_{\text{out}}^2,$$
$$\rho\sigma^2 = \rho_{\text{in}}\sigma_{\text{in}}^2 + \rho_{\text{out}}\sigma_{\text{out}}^2. \tag{A1}$$

Notably, Fig. 12(c) displays the computed *oblate* deformation and internal flow patterns in a drop, where top and bottom halves reveal results that are obtained by adopting interpolation 1 [Eq. (29)] and interpolation 2 [Eq. (A1)], respectively, at $\text{Ca}_E = 0.18$, $\varepsilon_{\text{in}}/\varepsilon_{\text{out}} = 10$, $\sigma_{\text{in}}/\sigma_{\text{out}} = 1.81$. Importantly, the generated error for deformation rate D by using above two interpolation schemes is 1.33%, and two schemes are clearly noted to induce the same internal flow pattern [Fig. 12(c)]. Additionally, Fig. 12(d) presents computed corresponding interfacial tangential electrical stresses [using Eqs. (29) and (A1)], which are quite identical. Such evidences clearly demonstrate that the density interpolation formula [Eq. (29)] utilized in the present work has little effect on the numerical results.

APPENDIX B: SPURIOUS CURRENTS

The spurious current is a commonly encountered problem [15,34,39,47] for many of the multiphase flow models involving curved interfaces. When a droplet is suspended in an immiscible fluid, the pressure difference between inside and outside the drop is balanced by surface tension. However, due to numerical error from inadequate discretization, when calculating corresponding gradient, the balance between pressure difference and surface tension is often not fully realized, causing spurious eddies [39] to be present in the vicinity of the interface. Accordingly, it becomes difficult to distinguish the physical flow from spurious eddies [39,47] when the spurious current is as large as the characteristic velocity of the problem. Therefore, it is essential to reduce the strength of spurious eddies. For this, in the absence of any body force (e.g., electric force), we run two cases to study the evolution of a drop by using Shan and Chen [33] model and the present explicit forcing model [34] until it reached static state. Figures 13(a) and 13(b) show the presence of corresponding spurious currents in the drop in the form of eight eddies [39]. The pink arrow and the level in each case denote the relative magnitude of fluid velocity. The length of arrows in Figs. 13(a) and 13(b) clearly show that the spurious current is reduced by a factor of 5.5 (see Ref. [39]) by the present model. Such results clearly demonstrate that, compared with the magnitude [e.g., Fig. 12(c)] of physical eddies, the present model drastically reduce the magnitude of spurious current with respect

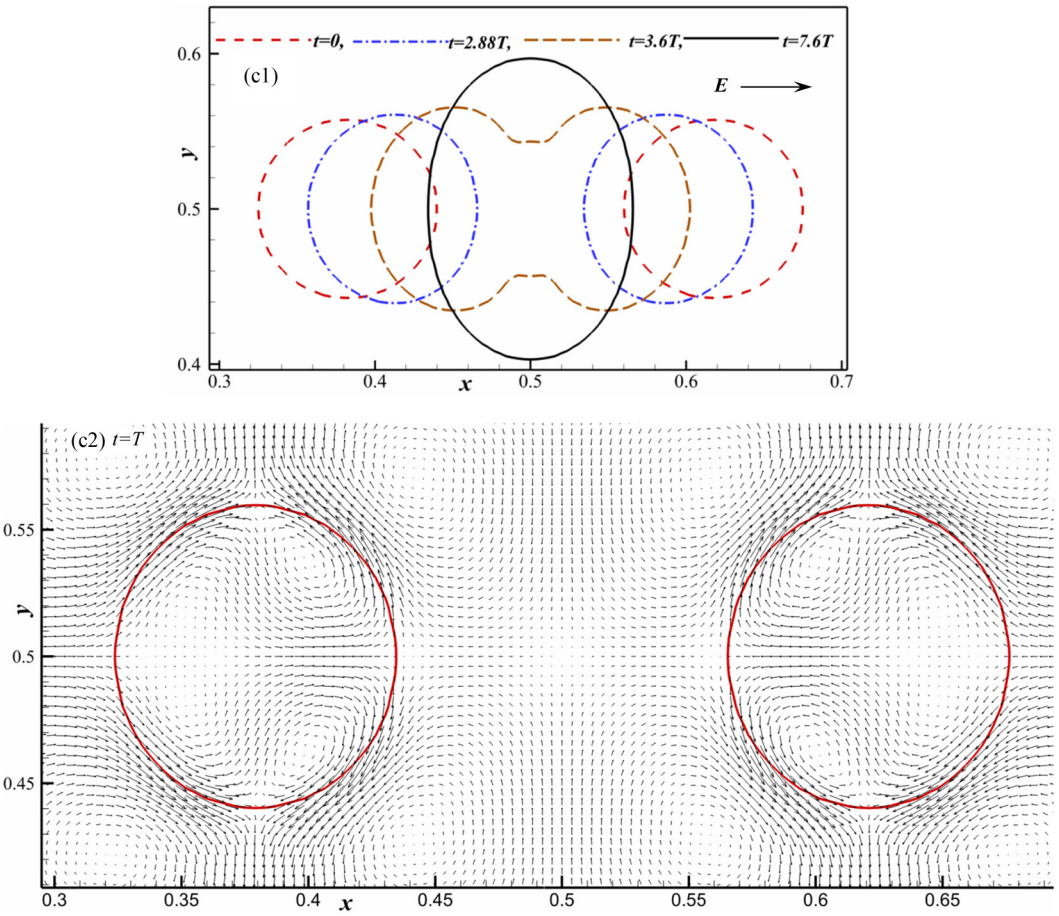

FIG. 14. The simulated (c1) *oblate* deformation of a drop pair ($\alpha = 0^\circ$) and the clear *nonbreaking* electrocoalescence that occurred at a reduced $\mathrm{Ca}_E = 0.33$, and for $\varepsilon_{\mathrm{in}}/\varepsilon_{\mathrm{out}} = 15.0$, $\sigma_{\mathrm{in}}/\sigma_{\mathrm{out}} = 5.0$, $\mathrm{Re} = 1.94$ [when $\varepsilon_{\mathrm{in}}/\varepsilon_{\mathrm{out}} > (\varepsilon_{\mathrm{in}}/\varepsilon_{\mathrm{out}})_{\mathrm{crit3}} = 9.57$]; and (c2) the induced surrounding velocity field at $t = T$ that facilitate the drop pair to move closer, while the surrounding vortical flow behavior unfolds supporting role of the developed *outflow*-natured upward and downward moving two dominant *outer vortex pairs* that dictate a drop to elongate vertically. Note that, at this lower $\mathrm{Ca}_E = 0.33$ the coalesced drop do not break, as the *outflow*-type two outer vortex pair could not create sufficient vertically opposite thrust.

to spurious current [Fig. 13(b)] generated by Shan and Chen [33] model. Therefore, the adopted model has the ability to better predict the actual nature of EHD flows.

APPENDIX C: NONBREAKING *OBLATE* COALESCENCE

Remarkably, it has been observed that, a nonbreaking *oblate*-shaped stable electrocoalescence is indeed achievable for $\varepsilon_{\mathrm{in}}/\varepsilon_{\mathrm{out}} = 15 > (\varepsilon_{\mathrm{in}}/\varepsilon_{\mathrm{out}})_{\mathrm{crit3}} = 9.57$ at fixed $\sigma_{\mathrm{in}}/\sigma_{\mathrm{out}} = 5.0$, by reducing the electric capillary number to $\mathrm{Ca}_E = 0.33$. For clarity, such a simulated scenario is presented in Fig. 14(c1) and 14(c2); revealing in detail the transient process of electrocoalescence [Fig. 14(c1)] and the role of the developed *outflow*-natured two near-interfacial outer vortex pairs (at $t = T$) in vertical drop elongation [Fig. 14(c2)]. In addition, as evident from Fig. 14(c2), the horizontal component of interactive near-field (including inner and outer regions) velocity clearly influences

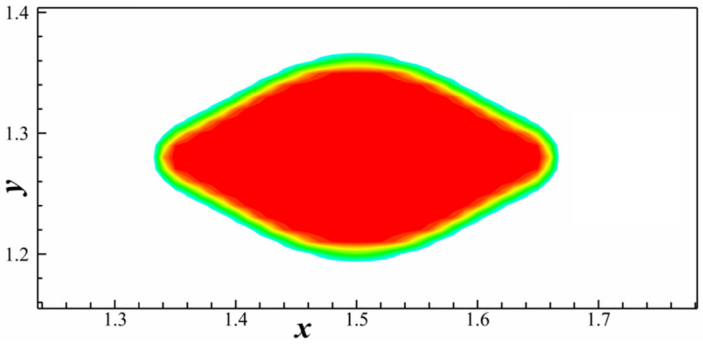

FIG. 15. Simulated Taylor cone formation for a single high-conductivity leaky drop. $\sigma_{in}/\sigma_{out} = 30.0$, $\varepsilon_{in}/\varepsilon_{out} = 1.37$, and $Ca_E = 0.68$.

the drop pair to move closer. Noteworthy also that, the *outflow*-type outer vortex pairs-induced flow around an *oblate* drop remains consistently [26] directed from *pole to equator*.

APPENDIX D: FORMATION OF TAYLOR CONE FOR A SINGLE LEAKY DIELECTRIC DROP IN A STRONG ELECTRIC FIELD

Taylor cone is clearly observed in perfect conductor (e.g., water) and perfect dielectrics (air bubble, methanol drop) on which only the normal electric stress acts [6,61]. Accordingly, plenty of charge is accumulated at two droplet tips that induce a high electric pressure, and is balanced by the interactive capillary stress around the higher curvature tip region (Taylor cone). However, for a leaky dielectric drop, in addition to electric pressure, the electric tangential stress is developed; which prevents formation of sharp conical tips [6]. Hereby, for increased conductivity of a leaky dielectric drop placed in a strong electric field, the Taylor cone formation in a way similar to conducting drops (e.g., Fig. 1 in Ref. [61]; Fig. 4c in Ref. [62]) is predicted prior to the drop breakup. Figure 15 presents such a simulated scenario at $\sigma_{in}/\sigma_{out} = 30.0$, $\varepsilon_{in}/\varepsilon_{out} = 1.37$ and $Ca_E = 0.68$. Note that, as discussed by Collins *et al.* [6], unlike the conducting case, the tip of a breaking leaky film/drop loses its conical shape and appear curved, as tip streaming initiates. However, the simulated detailed breaking events for a leaky drop are planned to be presented in a separate work, including their precise dependence on the viscosity ratio [62].

[1] P. Suemar, E. F. Fonseca, R. C. Coutinho, F. Machado, F. Fontes, L. C. Ferreira, E. L. Lima, P. L. Melo, J. C. Pinto, and M. Nele, Quantitative evaluation of the efficiency of water-in-crude-oil emulsion dehydration by electrocoalescence in pilot-plant and full-scale units, Ind. Eng. Chem. Res. **51**, 13423 (2012).

[2] C. R. Vigo and D. D. Ristenpart, Aggregation and coalescence of oil droplets in water via electrohydrodynamic flows, Langmuir **26**, 10703 (2010).

[3] J. Ogata and A. Yabe, Augmentation of boiling heat transfer by utilizing the EHD effect—EHD behavior of boiling bubbles and heat transfer characteristics, Int. J. Heat Mass Transfer **36**, 783 (1993).

[4] P. D. Marco, W. Grassi, G. Memoli, T. Takamasa, A. Tomiyama, and S. Hosokawa, Influence of electric field on single gas-bubble growth and detachment in microgravity, Int. J. Multiphase Flow **29**, 559 (2003).

[5] J. W. Xie, L. K. Lim, Y. Y. Phua, J. S. Hua, and C. H. Wang, Electrohydrodynamic atomization for biodegradable polymeric particle production, J. Colloid Interface Sci. **302**, 103 (2006).

[6] R. T. Collins, J. J. Jones, M. T. Harris, and O. A. Basaran, Electrohydrodynamic tip streaming and emission of charged drops from liquid cones, Nature Phys. **4**, 149 (2008).
[7] J. B. Fenn, M. Mann, C. K. Wong, and C. M. Whitehouse, Electrospray ionization for mass spectroscopy of large biomolecules, Science **246**, 64 (1989).
[8] K. Ahn, J. Agresti, H. Chong, M. Marquez, and D. A. Weitz, Electrocoalescence of drops synchronized by size-dependent flow in microfluidic channels, Appl. Phys. Lett. **88**, 264105 (2006).
[9] G. Taylor, Study in electrohydrodynamics. I. The circulation produced in a drop by electric field, Proc. R. Soc. Lond. A. **291**, 159 (1966).
[10] S. Torza, R. G. Cox, and S. G. Mason, Electrohydrodynamic deformation and burst of liquid droplets, Phil. Trans. R. Soc. Lond. A. **269**, 295 (1971).
[11] O. O. Ajayi, A note on Taylor's electrohydrodynamic theory, Proc. R. Soc. Lond. A **364**, 499 (1978).
[12] E. Lac and G. M. Homsy, Axisymmetric deformation and stability of viscous droplet in a steady electric field, J. Fluid Mech. **590**, 239 (2007).
[13] J. Zhang and D. Y. Kwok, A 2D lattice Boltzmann study on electrohydrodynamic droplet deformation with the leaky dielectric theory, J. Comput. Phys. **206**, 150 (2005).
[14] G. Tomar, D. Gerlach, G. Biswas, N. Alleborn, A. Sharma, F. Durst, S. W. J. Welch, and A. Delgado, Two-phase electrohydrodynamic simulation using a volume of fluid approach, J. Comput. Phys. **227**, 1267 (2007).
[15] J. Hua, L. K. Lim, and C. H. Wang, Numerical simulation of deformation/motion of a drop suspended in viscous liquids under influence of steady electric field, Phys. Fluids **20**, 113302 (2008).
[16] J. Q. Feng, A 2D electrohydrodynamic model for electrorotation of fluid drops, J. Colloid Interface Sci. **246**, 112 (2002).
[17] R. V. Craster and O. K. Matar, Electrically induced pattern formation in thin leaky dielectric films, Phys. Fluids **17**, 032104 (2005).
[18] P. F. Salipante and P. M. Vlahovska, Electrohydrodynamics of drops in strong uniform dc electric fields, Phys. Fluids **22**, 112110 (2010).
[19] H. Song, D. L. Chen, and R. F. Ismagilov, Reactions in droplets in microfluidic channel, Angew. Chem. Int. Ed. **45**, 7336 (2006).
[20] H. A. Pohl, *Dielectrophoresis* (Cambridge University Press, Cambridge, 1978).
[21] P. Atten, Electrocoalescence of water droplets in an insulating liquid, J. Electrost. **30**, 259 (1993).
[22] P. Atten, L. Lundgaard, and G. Berg, A simplified model of electrocoalescence of two close water droplets in oil, J. Electrost. **64**, 550 (2006).
[23] J. C. Bird, W. D. William, A. Belmonte, and H. A. Stone, Critical Angle for Electrically Driven Coalescence of Two Conical Droplets, Phys. Rev. Lett. **103**, 164502 (2009).
[24] J. S. Eow and M. Ghadiri, Drop-drop coalescence in an electric field: The effects of applied electric field and electrode geometry, Colloid. Surf. A **219**, 253 (2003).
[25] S. Mhatre, S. Deshmukh, and R. M. Thaokar, Electrocoalescence of a droplet pair, Phys. Fluids **27**, 092106 (2015).
[26] J. C. Baygents, N. J. Rivette, and H. A. Stone, Electrohydrodynamic deformation and interaction of droplet pairs, J. Fluid Mech. **368**, 359 (1998).
[27] X. Zhang, O. A. Basaran, and R. M. Wham, Theoretical prediction of electric field-enhanced coalescence of spherical droplets, AIChE J. **41**, 1629 (1995).
[28] P. R. Brazier-Smith, Stability and shape of isolated and pairs of water drops in an electric field, Phys. Fluids **14**, 1 (1971).
[29] P. R. Brazier-Smith, S. G. Jennings, and J. Latham, An investigation of the behaviour of drops and drop pairs subjected to strong electrical forces, Proc. R. Soc. Lond. A **325**, 363 (1971).
[30] G. I. Taylor, The coalescence of closely spaced drops when they are at different electric potentials, Proc. R. Soc. Lond. A **306**, 423 (1968).
[31] J. R. Castrejon-Pita, E. S. Betton, K. J. Kubiak, M. C. T. Wilson, and I. M. Hutchings, The dynamics of the impact and coalescence of droplets on a solid surface, Biomicrofluidics **5**, 014112 (2011).
[32] A. L. Kupershtokh and D. A. Medvedev, Lattice Boltzmann equation method in electrohydrodynamic problems, J. Electrostst. **64**, 581 (2006).

[33] X. Shan and H. Chen, Lattice-Boltzmann model for simulating flows with multiple phases and components, Phys. Rev. E **47**, 1815 (1993).
[34] M. L. Porter, E. T. Coon, Q. Kang, J. D. Moulton, and J. W. Carey, Multicomponent interparticle potential lattice Boltzmann model for fluids with large viscosity ratios, Phys. Rev. E **86**, 036701 (2012).
[35] J. R. Melcher and G. I. Taylor, Electrohydrodynamics: A review of the role of interfacial shear stresses, Annu. Rev. Fluid Mech. **1**, 111 (1969).
[36] D. Debasish and S. David, Electrohydrodynamics of viscous drops in strong electric fields: Numerical simulations, J. Fluid Mech. **829**, 127 (2017).
[37] D. A. Saville, Electrohydrodynamics: The Taylor-Melcher leaky dielectric model, Annu. Rev. Fluid Mech. **29**, 27 (1997).
[38] M. Chiesa, J. A. Melheim, A. Pedersen, S. Ingebrigtsen, and G. Berg, Force acting on water droplets falling in oil under the influence of an electric field: Numerical prediction versus experimental observation, Euro. J. Mech. B **24**, 717 (2005).
[39] Q. Li, K. H. Luo, Q. J. Kang, Y. L. He, Q. Chen, and Q. Liu, Lattice Boltzmann method method for multiphase flow and phase-change heat transfer, Prog. Energy Combust. Sci. **52**, 62 (2016).
[40] Q. Kang, D. Zhang, and S. Chen, Displacement of a two-dimensional immiscible droplet in a channel, Phys. Fluids **14**, 3203 (2002).
[41] S. Hou, X. Shan, Q. Zou, G. D. Doolen, and W. E. Soll, Evaluation of two lattice Boltzmann method for multiphase flows, J. Comput. Phys. **138**, 695 (1997).
[42] Q. Kang, D. Zhang, and S. Chen, Displacement of a three-dimensional immiscible droplet in a duct, J. Fluid Mech. **545**, 41 (2005).
[43] N. S. Martys and H. Chen, Simulation of multicomponent fluids in complex three-dimensional geometries by the lattice Boltzmann method, Phys. Rev. E **53**, 743 (1996).
[44] X. He and N. Li, Lattice Boltzmann simulation of electrochemical system, Comput. Phys. Commun. **129**, 158 (2000).
[45] Z. Guo, T. S. Zhao, and Y. Shi, A lattice Boltzmann algorithm for electro-osmotic flows in microfluidic devices, J. Chem. Phys. **122**, 144907 (2005).
[46] S. Succi, *The Lattice Boltzmann Equation* (Oxford University Press, Oxford, 2001).
[47] L. Chen, Q. J. Kang, Y. T. Mu, Y. L. He, and W. Q. Tao, A critical review of the pseudopotential multiphase lattice Boltzmann model: Method and application, Int. J. Heat Mass Trans. **76**, 210 (2014).
[48] M. R. Swift, W. R. Osborn, and J. M. Yeomans, Lattice Boltzmann simulation of nonideal fluids, Phys. Rev. Lett. **75**, 830 (1995).
[49] J. Q. Feng and T. C. Scott, A computational analysis of electrohydrodynamics of a leaky dielectric drop in an electric field, J. Fluid Mech. **311**, 289 (1996).
[50] H. Paknemat, A. R. Pishevar, and P. Pournaderi, Numerical simulation of drop deformations and breakup modes caused by direct current electric fields, Phys. Fluids **24**, 102101 (2012).
[51] C. Sozou, Electrohydrodynamics of a pair of liquid drops, J. Fluid Mech. **91**, 541 (1975).
[52] K. B. M. Q. Zaman, Axis switching and spreading of an asymmetric jet: The role of coherent structure dynamics, J. Fluid Mech. **316**, 1 (1996).
[53] A. Sau, Vortex dynamics and mass entrainment in a rectangular channel with a suddenly expanded and contracted part, Phys. Fluids **14**, 3280 (2002).
[54] A. Sau, Generation of streamwise vortices in square sudden-expansion flows, Phys. Rev. E **69**, 056307 (2004).
[55] A. Sau, Role of streamwise dynamics in spreading and mixing of flows through a rectangular sudden expansion, Phys. Fluids **23**, 083602 (2011).
[56] Q. Dong and A. Sau, Microphysics of mass-transport in coupled droplet-pairs at low Reynolds number and the role of convective dynamics, Phys. Fluids **28**, 063602 (2016).
[57] J. D. Chen, A model of coalescence between two equal-sized spherical drops or bubbles, J. Colloid Interface Sci. **107**, 209 (1985).
[58] Y. Lin, P. Skjetne, and A. Carlson, A phase field model for multiphase electro-hydrodynamic flow, Int. J. Multiphase Flow **45**, 1 (2012).

[59] P. T. Yue, J. J. Feng, C. Liu, and J. Shen, A diffuse-interface method for simulating two-phase flows of complex fluids, J. Fluid Mech. **515**, 293 (2004).

[60] J. J. Feng, C. Liu, J. Shen, and P. Yue, An energetic variational formulation with phase field methods for interfacial dynamics of complex fluids: advantages and challenges, *Modeling of Soft Matter*, The IMA Volumes in Mathematics and its Applications, Vol. 141, edited by MC. T. Calderer and E. M. Terentjev (Springer, New York, NY, 2005) pp. 1–26.

[61] J. F. F. de la Mora, The fluid dynamics of Taylor cones, Annu. Rev. Fluid Mech. **39**, 217 (2007).

[62] R. B. Karyappa, S. Deshmukh, and R. M. Thaokar, Breakup of a conducting drop in a uniform electric field, J. Fluid Mech. **754**, 550 (2014).